Inositol pyrophosphate profiling reveals regulatory roles of IP6K2-dependent enhanced IP_7 metabolism in enteric nervous system

Masatoshi Ito[1,*], Natsuko Fujii[2], Saori Kohara[2], Shuho Hori[1], Masayuki Tanaka[1], Christopher Wittwer[7], Kenta Kikuchi[6], Takatoshi Iijima[3], Yu Kakimoto[4], Kenichi Hirabayashi[5], Daisuke Kurotaki[6], Henning J. Jessen[7], Adolfo Saiardi[8], Eiichiro Nagata[2,*]

[1]Support Center for Medical Research and Education, Tokai University, 143 Shimokasuya, Isehara, Kanagawa 259-1193, Japan

[2]Department of Neurology, Tokai University School of Medicine, 143 Shimokasuya, Isehara, Kanagawa 259-1193, Japan

[3]Department of Molecular Life Science, Tokai University School of Medicine, 143 Shimokasuya, Isehara, Kanagawa 259-1193, Japan

[4]Department of Forensic Medicine, Tokai University School of Medicine, 143 Shimokasuya, Isehara, Kanagawa 259-1193, Japan

[5]Department of Pathology, Tokai University School of Medicine, 143 Shimokasuya, Isehara, Kanagawa 259-1193, Japan

[6]Laboratory of Chromatin Organization in Immune Cell Development, International Research Center for Medical Sciences, Kumamoto University, 2-2-1 Honjo, Chuo-ku, Kumamoto, Kumamoto 860-0811, Japan

[7]Institute of Organic Chemistry, University of Freiburg, Albert str. 21, 79104, Freiburg, Germany

[8]Medical Research Council Laboratory for Molecular Cell Biology, University College London, WC1E 6BT, London, UK

* Correspondence:

Eiichiro Nagata, M.D., Ph.D.

Department of Neurology, Tokai University School of Medicine, 143 Shimokasuya, Isehara, Kanagawa 259-1193, Japan

TEL: +81-463-93-1121 (ext. 2242); FAX: +81-463-92-6299; e-mail: enagata@is.icc.u-tokai.ac.jp

Masatoshi Ito, Ph.D.

Support Center for Medical Research and Education, Tokai University, 143 Shimokasuya, Isehara, Kanagawa 259-1193, Japan

TEL: +81-463-93-1121 (ext. 2553); e-mail: masa104-ito@tokai-u.jp

Abstract

Inositol pyrophosphates (PP-IPs) regulate diverse physiological processes; to better understand their functional roles, assessing their tissue-specific distribution is important. Here, we profiled PP-IP levels in mammalian organs using a novel HILIC-MS/MS protocol and discovered that the gastrointestinal tract (GIT) contained the highest levels of IP_7 and its precursor IP_6. Although their absolute levels in the GIT is diet-dependent, elevated IP_7 metabolism still exists under dietary regimes devoid of exogenous IP_7. Of the major GIT cells, enteric neurons selectively express the IP_7-synthesizing enzyme IP6K2. *IP6K2*-knockout mice exhibited significantly impaired IP_7 metabolism in the various organs including the proximal GIT. Additionally, HILIC-MS/MS analysis displayed that genetic ablation of *IP6K2* significantly impaired IP_7 metabolism in the gut and duodenal muscularis externa containing myenteric plexus. Whole transcriptome analysis of duodenal muscularis externa further suggested that IP6K2 inhibition induced the gene sets associated with mature neurons such as inhibitory, GABAergic and dopaminergic neurons, concomitantly with suppression of those for neural progenitor/stem cells and glial cells. In addition, IP6K2 inhibition explicitly affected transcript levels of certain genes modulating neuronal differentiation and functioning, implying critical roles of IP6K2-IP_7 axis in developmental and functional regulation of enteric nervous system. These results collectively reveal an unexpected role of mammalian IP_7—a highly active IP6K2-IP_7 pathway is conducive to enteric nervous system.

Keywords: inositol pyrophosphate, diphosphoinositol pentakisphosphate, inositol hexakisphosphate kinase 2, hydrophilic interaction liquid chromatography-tandem mass

63 spectrometry, enteric nervous system

64

Introduction

Myo-inositol phosphates (IPs) are ubiquitously synthesized in all organisms and are involved in pleiotropic biological processes, most importantly in intracellular signaling (Irvine and Schell, 2001). Among the IP family, inositol hexakisphosphate (IP_6) is the most abundant, and serves as a precursor of inositol pyrophosphates (PP-IPs) possessing diphosphate moieties at specific carbon positions (Saiardi, 2012; Wilson et al, 2013; Shears, 2015; Shah et al, 2017). Diphosphoinositol pentakisphosphate (IP_7) and bisdiphosphoinositol tetrakisphosphate (IP_8) are the most well-characterized PP-IPs in mammals and yeasts, and carry diphosphate moieties at the 5-position (5-IP_7) and 1,5-positions (1,5-IP_8) of the inositol ring, respectively (Draskovic et al, 2008; Shears, 2015). Recent studies using mammalian cells have demonstrated that PP-IPs regulate phosphate flux, energy homeostasis, and post-transcriptional processes at the molecular level (Wilson et al, 2019; Li et al, 2020; López-Sánchez et al, 2020; Sahu et al, 2020; Gu et al, 2021). In mammals, 5-IP_7 is synthesized by three inositol hexakisphosphate kinases (IP6Ks) IP6K1, IP6K2, and IP6K3. IP6K1 and IP6K2 are expressed in most mammalian tissues, with highest expression in the brain and testis, whereas IP6K3 expression is mainly restricted to the muscles (Saiardi et al, 2001; Moritoh et al, 2016; Laha et al, 2021). *In vivo* studies using *IP6K1*- or *IP6K2*-knockout mice suggest that PP-IPs contribute to the development and maintenance of neuronal cells (Fu et al, 2017; Nagpal et al, 2018, 2021). In addition to these *in vivo* mice studies, our as well as other research groups have shown that PP-IPs are pathophysiologically involved in the progression of obesity (Chakraborty et al, 2010; Ghoshal et al, 2016), in cancer (Rao et al, 2015) and in neurodegenerative disorders such as Huntington's disease (Nagata et al, 2011), amyotrophic lateral sclerosis (Nagata et al, 2016), and Alzheimer's disease

(Crocco et al, 2016). Therefore, PP-IPs are currently being considered as potential therapeutic targets for several diverse human disorders (Shears, 2016; Chakraborty, 2018). However, we are unaware of any systematic studies that have directly and comprehensively analyzed PP-IP distribution in mammalian tissues, which could provide valuable insights into the effects of pharmacological interventions on the PP-IP system.

Over the past decade, extensive efforts have been made to develop analytical methods for detecting PP-IPs. Traditionally, PP-IPs have been studied using radioisotopic ^{3}H-inositol labeling coupled with anion exchange chromatography (Azevedo and Saiardi, 2006), which allows sensitive detection of metabolically labeled PP-IPs from cultured cells. Electrophoretic separation and colorimetric visualization of PP-IPs (Losito et al, 2009) have also become alternative standard methods for distinguishing PP-IPs. However, PP-IPs in mammalian tissues can neither be radioisotopically labelled, nor explicitly detected using colorimetric visualization. A mass spectrometric method coupled with capillary electrophoretic separation (capillary electrophoresis-mass spectrometry, CE-MS) (Qiu et al, 2020) was recently reported for sensitive analysis of PP-IPs in biological samples at the isomer level. However, the instrument setup involved is complex and requires skillful handling, and is therefore rarely available in research institutes.

We recently developed an analytical method that directly detects mammalian-derived IP_7 and its precursor IP_6 using conventional liquid chromatography-tandem mass spectrometry (LC-MS/MS) coupled with hydrophilic interaction liquid chromatography (HILIC) (Ito et al, 2018), enabling the previously impossible quantitation of PP-IPs in mammalian tissues. In this study, we analyzed

PP-IP and their precursor IP_6 levels in mammalian organs using a refined HILIC-MS/MS protocol. We found that IP_7 was present at explicit levels in the mammalian central nervous system (CNS), where IP6Ks are highly expressed. Surprisingly, we also discovered that the highest IP_7 production was observed in the gastrointestinal tract (GIT), even after depletion of dietary derived IP_7. Of the major GIT cells, enteric neurons selectively expressed IP_7-synthesizing enzyme IP6K2, which was revealed by assessment of single cell RNA-sequencing (scRNA-seq) data sets and confirmed by immunohistochemical detection. Our HILIC-MS/MS survey using *IP6K2*-knockout (*IP6K2*$^{-/-}$) mice exhibited that IP6K2-dependent enhanced IP_7 metabolism exists in the gut and duodenal muscularis externa where myenteric plexus is located. We further performed whole transcriptome analysis of *IP6K2*-deficient and wild type (WT) duodenal muscularis externa to define a physiological role of IP6K2-IP_7 pathway in enteric nervous system (ENS).

Results

Refinement of HILIC-MS/MS protocol for PP-IP analysis

Before investigating PP-IP metabolism in mammalian tissues, we improved our HILIC-MS/MS analysis protocol for unequivocal detection and more precise quantitation of PP-IPs. Medronic acid compatible with LC-MS analysis significantly improves the chromatographic peak shape of phosphorylated compounds (Hsiao et al, 2018). We employed a form of this solvent additive that has been optimized for HILIC analysis (InfinityLab deactivator additive, Agilent Technologies) and found that using it significantly improved the peak shapes of IP_6 and IP_7 (Fig. 1A), whereas without the additive, remarkably poor IP_6 and IP_7 peak shapes were obtained, probably due to the cumulative adsorption of cationic contaminants on the column derivative (amino group). Chromatographic peaks of IP_7 levels as low as 10 pmol were discernible using this additive (Fig. 1B). Direct use of LC-MS grade medronic acid resulted in similar beneficial effects on IP_6 and IP_7 peaks (Fig. S1), but the background noise was relatively higher than that for the InfinityLab deactivator additive. Thus, the additive was used in all our subsequent analyses.

To quantitate IP_8 (Fig. 1C) simultaneously with IP_6 and IP_7, we assessed the mass spectra of IP_8 fragment ions obtained by collision-induced dissociation of the synthetic IP_8 standard (Fig. 1D). A series of fragment ions representing the losses of phosphate (80 Da) and water (18 Da) appeared in the spectra. Based on this result, we assigned each IP_8 fragment and optimized the selected reaction monitoring (SRM) conditions (Table S1). Using chemical standards of PP-IPs and their precursor IP_6, we observed chromatographic peaks of IP_6, IP_7, and IP_8 at regular intervals of 0.2 min (Fig. 1E). To benchmark this method for the detection of endogenous PP-IPs, we treated HCT116

cells with NaF, which is known to increase IP_7 level (Menniti et al, 1993). While a clear IP_6 SRM peak and subtle IP_7 and IP_8 SRM peaks were observed for untreated HCT116 cells, explicit IP_7 and IP_8 SRM peaks were detected for NaF-treated cells (Fig. 1F). We also observed a dose-dependent reduction in IP_7 level and the IP_7/IP_6 ratio in HCT116 cells treated with the IP6K inhibitor TNP (Fig. S2). Thus, our refined HILIC-MS/MS protocol achieved robust, sensitive, and reliable detection of endogenous IP_6, IP_7, and IP_8 in biological samples.

The mammalian gastrointestinal tract (GIT) contains high levels of PP-IPs

Using the newly developed HILIC-MS/MS protocol, we investigated the distribution of PP-IPs in experimental model rodents fed with a standard plant-based diet (CE-2; Clea, Japan). Fifteen organs, including the CNS and GIT, were harvested from standard diet-fed C57BL/6J male mice. Surprisingly, HILIC-MS/MS analysis showed that the GIT had the highest levels of IP_6 and IP_7, even after extensive rinsing of the organs with phosphate-buffered saline (PBS) to wash out the digested contents (Fig. 2A, B and Table S2). Importantly, the IP_7/IP_6 ratio in the GIT was remarkably high, by far the highest in all organs examined (Fig. 2C and Table S2). A subtle IP_8 SRM peak was detected in stomach and small intestine samples, wherein IP_7 was abundant (Fig. 2D) but was not detected in other organs. While IP_7 SRM peaks were clearly detected in CNS samples (Fig. 2E), IP_7 levels in the CNS were modest compared with those in the GIT. Moreover, the IP_7/IP_6 ratio in the spinal cord appeared to be higher than that in the cerebrum (Fig. 2C).

Several reports have shown that IPs (mainly IP_6, known as phytic acid) are present in a variety of crop seeds (Dorsch et al, 2003; Liu et al, 2009; Kolozsvari et al, 2015;

Duong et al, 2017); moreover, plants also generate PP-IPs, which are crucial for phosphorus-starvation responses (Dong et al, 2019; Ried et al, 2021; Riemer et al, 2021). Therefore, we assumed that the plant-based CE-2 diet contains IP_6 and PP-IPs, and explicit chromatographic peaks of IP_6, IP_7, and IP_8 were observed in CE-2 samples (Fig. 2F, upper panels). The concentrations of IP_6 and IP_7 in CE-2 were 3.96 ± 0.82 nmol/mg and 0.17 ± 0.03 nmol/mg, respectively. We next investigated their concentrations in purified diets with minimal levels of plant-derived components (Fig. 2F, middle and lower panels). The two purified diets examined (iVid-neo and 70% casein) contained low amounts of IP_6 and negligible amounts of IP_7 and IP_8. Quantitative analysis revealed that the levels of all PP-IPs in both purified diets were less than 2% of those in CE-2 (Fig. 2G).

Since the IP_7/IP_6 ratios in the stomach and duodenum were significantly higher than that in CE-2 (Fig. 2C), the high IP_7 level detected could not be attributed to its direct absorption from CE-2 diet, so it must have been endogenously produced by active IP6K enzyme. However, to exclude the possibility of selective intestinal absorption of IP_7, we analyzed the feces of mice fed on CE-2 and estimated the loss of IP_6 and IP_7 in the digestive system (Fig. 2H). Similar to those for CE-2 samples, IP_6 and IP_7 SRM peaks were clearly observed in mouse feces samples. Quantitative analysis showed that approximately 50% of IP_6 and IP_7 in ingested food remained in the feces (Fig. 2I). Since the IP_7/IP_6 ratio remained unchanged between undigested CE-2 and feces, we could exclude that IP_7 is selectively absorbed in the GIT, further demonstrating that the abundant IP_7 levels observed in the GIT must be endogenously generated by cellular metabolism.

Enhanced IP_7 metabolism is retained in the proximal GIT of rodents under conditions of depleted dietary IP_6 and PP-IP supply

To validate the presence of endogenously synthesized PP-IPs in the GIT, C57BL/6J mice were fed for 2 months on standard CE-2 diet; on iVid-neo containing negligible amounts of IP_6 and PP-IPs (Fig. 2E); or left fasting for 48 h (Fig. 3A). The GIT of both purified diet-fed and fasted mice showed a reduction in IP_6 and IP_7 levels compared with those of standard diet-fed mice; however, the levels were still close to (in the case of IP_6) or far greater than (in the case of IP_7) the CNS levels (Fig. 3B and C). IP_8 was not detected in any of the tested organs of purified diet-fed and fasted mice. The SRM chromatograms of both purified diet-fed and fasted mice samples had explicit IP_7 SRM peaks (Fig. 3D). Importantly, the stomach and duodenum of these mice showed prominently higher IP_7/IP_6 ratio than those of their standard diet-fed counterparts (Fig. 3E), implying further enhanced IP_7 metabolism compensated for the overall reduced IP_7 level. On the other hand, both purified diet-fed and fasted mice did not show any changes in the IP_6 and IP_7 levels as well as the IP_7/IP_6 ratio in the CNS and testis compared with those of mice fed a standard diet. However, as with standard diet-fed mice, both purified diet-fed and fasted mice showed higher IP_7/IP_6 ratios in the spinal cord than in the cerebrum. We also investigated IP_7 levels in the GIT of purified diet (70% casein)-fed Sprague–Dawley rats (Fig. 3F). Analogous to the results observed in the mouse model, both IP_6 and IP_7 levels in the GIT of these rats were drastically reduced compared with those in the standard diet-fed GIT and comparable to those in the CNS (Fig. 3G and H). In addition, the IP_7/IP_6 ratio was higher in the stomach and duodenum of purified diet-fed rats compared with that of standard diet-fed rats (Fig. 3I), further demonstrating very active IP_7 metabolism in the mammalian proximal GIT.

Enteric neurons highly express IP6K2 in the mammalian GIT

To investigate the expression levels of the three IP6Ks in each GIT cell type, we used single-cell RNA sequencing (scRNA-seq) datasets and compared the expression levels of IP6Ks among GIT cell types. Quantitative analysis using a human embryonic intestinal cell scRNA-seq dataset (Fawkner-Corbett et al, 2021) showed that enteric neural cells expressed the highest levels of IP6K2 among different intestinal cells (Fig. 4A, left panel). In enteric neural cells, IP6K2 was selectively expressed across enteric neuron subsets, such as motor neurons, interneurons, and neuroendocrine cells, but not in glial cells (Fig. 4A, right panel). This analysis was further supported by the IP6K quantitation using both E15.5 (Fig. S3A) and E18.5 (Fig. 4B) mouse embryonic ENS scRNA-seq datasets (Morarach et al, 2021). As in humans, IP6K2 isoform expression level in mouse enteric neurons was higher than in other neural cells such as neuroblasts, progenitors, glial cells, and Schwann cells. Moreover, the transcriptional analysis-based data were verified using immunohistochemical analyses. IP6K2 colocalized with the neuronal marker HuC/D in the mouse duodenal muscle layer, suggesting IP6K2 was expressed in the myenteric plexus (Fig. 4C). Other than enteric neurons, several cell types, including secretory progenitor cells, also expressed relatively high levels of IP6K2 (Fig. S3B). In addition, mouse enteric epithelial cell scRNA-seq data (Haber et al, 2017) showed that IP6K2 is expressed in mouse enteroendocrine cells (Fig. S3C). Expression levels of IP6K1 and IP6K3 in entire embryonic intestinal cells were low and negligible, respectively (Fig. 4A and B). These results suggest that IP6K2 is highly expressed in mammalian enteric neurons.

IP6K2$^{-/-}$ mice show significant impairment of IP_7 metabolism in the proximal GIT

To estimate the importance of IP6K2 in endogenous IP_7 synthesis in the mammalian organs including GIT, we employed a genetically modified mouse in which *IP6K2* exon 6, encoding the kinase domain, was specifically deleted (Fig. 5A, upper panel) (Rao et al, 2014). To avoid any contamination of dietary-derived IPs in our analysis, *IP6K2*-knockout (*IP6K2*$^{-/-}$) or wild type (WT) mice raised on the standard CE-2 diet were switched to a purified diet (iVid-neo) for one week, and then fasted for 48 h before sacrifice (Fig. 5A, lower panel). In WT mice, IP6K2 mRNA containing the exon 6 sequence was expressed in the proximal GIT but only marginally compared with the expression in the CNS (Fig. 5B). As expected, the IP6K2 transcript was absent in *IP6K2*$^{-/-}$ mouse organs. We confirmed the loss of IP6K2 expression at the protein level using cerebrum lysate (Fig. 5C), because it has high IP6K2 protein expression and thus was useful for clearly validating the loss of IP6K2 in *IP6K2*$^{-/-}$ mice. HILIC-MS/MS analysis showed that *IP6K2*$^{-/-}$ mice had significantly lower levels of IP_7 in various organs, including the stomach and duodenum, compared with those in their WT counterparts, while IP_6 levels in each organ were almost the same between *IP6K2*$^{-/-}$ and WT mice (Fig. 5D and E). As previously observed (Fig. 3E and I), the IP_7/IP_6 ratios in the stomach and duodenum of WT mice were much higher than those in the other organs examined (Fig. 5F). On the other hand, the IP_7/IP_6 ratios in these two organs were significantly reduced in *IP6K2*$^{-/-}$ mice. The IP_7 SRM peaks for the *IP6K2*$^{-/-}$ mouse stomach and duodenum were also smaller compared with those of WT mice, while IP_6 levels were unchanged (Fig. 5G and H). Collectively, these data demonstrate that IP6K2 is required for enhanced IP_7 metabolism in the mammalian proximal GIT.

IP6K2-dependent enhanced IP_7 metabolism exists in the gut and duodenal muscularis externa where the myenteric plexus is located

Since IP_7-synthesizing kinase IP6K2 is selectively expressed in enteric neurons (Fig. 4), we next sought to investigate IP_7 metabolism in the mammalian ENS. To this end, we collected the stomach and the consecutive 5 cm segments of duodenum, jejunum, and ileum from standard diet-fed or fasted mice. Some of these organs collected were subsequently used to isolate the muscularis externa where the myenteric plexus is located. These total GIT tissues and their muscularis externa were subjected to HILIC-MS/MS analysis to compare their IP_7 metabolism (Fig. 6A). Similar to the results shown in Fig. 3, 48 h fasting of mice rendered drastic reduction of IP_6 and IP_7 levels with concomitant increase of IP_7/IP_6 ratio in total GIT tissues (Fig. 6B-D). Although the muscularis externa contained less IP_6 and IP_7 than total GIT tissues, the muscle layer exhibited a higher IP_7/IP_6 ratio than total GIT tissues, which was less dependent on dietary conditions. IP_7/IP_6 ratio of the duodenal muscularis externa was highest among the corresponding muscle layers of the neighboring GITs, implying highly active IP_7 metabolism in the duodenal ENS. To verify the relationship between IP6K2-IP_7 axis and ENS, we first attempted to visualize the duodenal myenteric plexus of *IP6K2*$^{-/-}$ mice by whole mount immunostaining (Fig. 6E). We found that *IP6K2* deletion largely affected neither the morphological features nor the neuronal cell density in the duodenal myenteric plexus (Fig. 6F). We next prepared the muscularis externa from the stomach to the ileum of WT and *IP6K2*$^{-/-}$ mice, first depleting dietary IP_7 in the GIT by 48 h fasting and performed HILIC-MS/MS analysis to evaluate IP_7 metabolism in the ENS of *IP6K2*$^{-/-}$ proximal GITs (Fig. 6G). While IP_6 levels in the muscularis externa were almost equivalent between WT and *IP6K2*$^{-/-}$ mice, IP_7 levels and IP_7/IP_6

297 ratios were significantly reduced in the gut and duodenal muscularis externa of *IP6K2*$^{-/-}$
298 mice (Fig. 6H-J). These results suggest that IP6K2 actively produces IP_7 in the gut and
299 duodenal muscularis externa where enteric neurons are concentrated.
300
301 **The IP6K2-IP_7 axis is crucial for certain neurotranscriptome profiles associated**
302 **with ENS development and functioning**
303 Considering the active IP6K2-IP_7 axis in the ENS, we assumed that alteration of IP_7
304 metabolism by *IP6K2* deletion might affect neuronal status in the proximal GIT. Thus,
305 we randomly selected two neuronal genes expressed in the GIT as well as the CNS
306 (Gremel et al, 2015), namely *dopamine receptor D5* (*Drd5*), and *cholecystokinin B*
307 *receptor* (*Cckbr*), and investigated their mRNA levels in both the CNS and GIT by
308 quantitative PCR (qPCR) (Fig. 7A). Compared with those in WT mice, these mRNA
309 levels were explicitly increased from the stomach through the small intestine of *IP6K2*$^{-/-}$
310 mice, especially in the duodenum, but not the colon and CNS. To comprehensively
311 appreciate the role of IP6K2-dependent IP_7 metabolism in neuronal gene regulation in
312 the mammalian ENS, we isolated the duodenal muscularis externa from WT and
313 *IP6K2*$^{-/-}$ mice and performed whole transcriptome analysis by RNA-sequencing
314 (RNA-seq) (Fig.7B). Gene set enrichment analysis (GSEA) showed that *IP6K2* deletion
315 suppressed certain gene sets associated with neural stem/progenitor cells,
316 oligodendrocyte progenitor cells, and glial cells, concomitantly with the induction of
317 those of mature neurons such as inhibitory, dopaminergic or GABAergic neurons (Fig.
318 7C, D and Data S1), implying that inhibition of the IP6K2-IP_7 pathway triggers
319 neurodevelopmental imbalance in the mammalian ENS. The RNA-seq analysis also
320 exhibited that 107 and 134 out of 23,405 genes were more than 1.5-fold increased or

decreased in *IP6K2*$^{-/-}$ with P-value less than 0.05, respectively (Fig. S4A). Pathway enrichment analysis of these genes showed that transcripts increased more than 1.5-fold in *IP6K2*$^{-/-}$ were significantly enriched for proteins involved in neuronal signaling (neuroactive ligand-receptor interaction of KEGG annotation) (Fig. S4B). In these transcripts, we observed that 7 genes associated with neuronal function (*Nckipsd*, and *Hrh4*) or development (*Noto*, *Tbx1*, *Tbx18*, *Pax7*, and *Mycn*) were prominently altered in their transcript levels between WT and *IP6K2*$^{-/-}$ (Fig. 7E). To validate our RNA-seq results, differential expression of these 7 neuronal genes were further assessed by qPCR and all of these candidate genes exhibited similar significant or prominent changes in transcript levels as observed in RNA-seq results (Fig. 7F). Quantitative PCR analysis also showed that expression of other neuronal genes, including *Drd5* and *Cckbr*, explicitly increased in *IP6K2*$^{-/-}$ duodenal muscularis externa (Fig. 7G). These changes were not observed in the RNA-seq analysis possibly because they were below the lower detection limit and/or quantitation error (Robert and Watson, 2015; Everaert et al, 2017). Collectively, the IP6K2-IP_7 axis contributes to certain neurotranscriptome profiles involved in ENS development and functioning.

Discussion

Mammalian PP-IPs have been implicated in obesity and diseases such as cancer and neurodegenerative disorders, and thus, their metabolism is a promising drug target (Shears, 2016; Chakraborty, 2018). For this reason, *in vivo* PP-IP profiling of mammalian tissues is an important subject of research. However, this objective has been thwarted by various technical difficulties. Recently, we developed an HILIC-MS/MS analysis protocol for the sensitive and specific detection of IP_7 and its precursor IP_6 (Ito et al, 2018). In this study, we quantified *in vivo* PP-IP levels in mammalian organs using a refined HILIC-MS/MS protocol and evaluated the contribution of IP6K2 to PP-IP metabolism by analyzing mice lacking this IP_7-synthesizing kinase.

We observed abundant IP_6 and a small but detectable quantity of IP_7 in various mammalian organs. Specifically, a discernible level of IP_7 was detected in the mammalian CNS. These results correlate with the fact that expression of the IP_7-synthesizing kinases IP6K1 and IP6K2 is ubiquitous and highest in the CNS (Saiardi et al, 2001; Moritoh et al, 2016; Laha et al, 2021). Since IP_7 levels in the CNS remain constant irrespective of dietary supply (Fig. 3C and H), it is plausible that food-derived IP_7 is not directly delivered to the CNS. In agreement with this idea, previous studies on rodents have reported that food-derived IPs are degraded in the GIT and released into the circulation as myo-inositol or inositol monophosphate (IP_1) (Sakamoto et al, 1993; Eiseman et al, 2011). There is also evidence that circulating plasma contains no higher order IPs, such as IP_6 (Wilson et al, 2015). Considering our observation that IP_7 levels were significantly decreased in the CNS of *IP6K2*$^{-/-}$ mice compared with those in WT counterparts (Fig. 5E), it is reasonable to regard the IP_7 detected in the CNS as endogenously generated. Intriguingly, the IP_7/IP_6 ratio in the

363 spinal cord was higher than those in the cerebrum and cerebellum, suggesting
364 heterogeneous IP_7 metabolic activity in the rostral and caudal CNS.

365 Surprisingly, we found that standard diet-fed rodents had far more IP_7 in the GIT than
366 in the CNS (Fig. 2B). Furthermore, the IP_7/IP_6 ratio, an indicator of PP-IPs metabolism,
367 was far higher in the GIT than in the CNS (Fig. 2C). The mouse diet affected the level
368 of IP_6 and IP_7 in the GIT but did not influence the high IP_7 metabolism, as revealed by
369 the IP_7/IP_6 ratio (Fig. 3E and I). The dietary influence on IP_6 and IP_7 levels in the GIT is
370 likely a direct consequence of the availability of inositol in plant-derived food (CE-2).
371 Some of this inositol could be generated from IP_6 by intestinal flora (Priyodip et al,
372 2017) and directly absorbed by inositol transporters such as SMIT1, SMIT2, and HMIT
373 (Schneider, 2015). A considerable amount of IP_7 was detected in the GIT of rodents
374 even when the supply of dietary PP-IPs was almost depleted (Fig. 3C and H). The
375 IP_7/IP_6 ratio was heterogeneous along the GIT but significantly higher in the proximal
376 GIT of these dietary PP-IP-depleted rodents (Fig. 3E and I), indicating that substantial
377 endogenous IP_7 metabolism occurs in the proximal GIT. Accordingly, IP_7 levels in the
378 stomach and duodenum were significantly diminished in *IP6K2*$^{-/-}$ mice under dietary
379 PP-IP-depleted conditions (Fig. 5E). Therefore, our HILIC-MS/MS analysis
380 unexpectedly revealed enhanced IP_7 metabolism in the mammalian GIT.

381 The GIT consists of several histological layers including the muscularis externa that
382 contains the myenteric plexus, a collection of large neuronal assemblies in the GIT. Our
383 HILIC-MS/MS survey of the proximal GIT clarified that the muscularis externa has a
384 higher IP_7/IP_6 ratio than whole GIT tissues, and the duodenal muscle layer has a much
385 higher IP_7/IP_6 ratio than those of neighboring GIT segments (Fig. 6D). Considering the
386 expression of the IP_7-synthesizing enzyme IP6K2 in the myenteric plexus (Fig. 4A-C)

and the significant decrease of IP_7/IP_6 ratio in *IP6K2*-deficient gut and duodenal muscle layers (Fig. 6J), these observations lead to the idea that IP6K2 actively synthesizes endogenous IP_7 in the ENS of the proximal GIT. Our results also implied the presence of endogenous IP_7 in other GIT layers since total GIT tissues of dietary IP_7-depleted (fasted) mice contained a greater amount of IP_7 than their corresponding muscle layers (Fig. 6C). Since another major nerve plexus exists in the submucosal layer (*i.e.* submucosal plexus), the submucosal layer may contain endogenous IP_7 to some extent. This PP-IP might also exist in mucosal epithelium because certain enteroendocrine cells, including Tuft cells, express IP6Ks at the relatively high level (Fig. S3B and C). Tuft cell is one of rare cell types present in intestinal epithelium. Park et al. recently showed that Tuft cell development is controlled by inositol polyphosphate multikinase (IPMK), an enzyme responsible for driving IP metabolic pathway leading to IP_7 synthesis (Park et al, 2022). This fact and our data (Fig. S3B and C) encourage to deem that IP6K2 and IP_7 might underlie Tuft cell physiology as well. Future study is required for assessing cell type-specific IP_7 metabolism both in enteric neurons as well as in other GIT cells to more precisely characterize IP_7 metabolism in the GIT.

Although *IP6K2* was initially cloned as a Pi uptake stimulator from a rabbit duodenum complementary DNA (cDNA) library (Norbis et al, 1997) and was annotated soon after as encoding an IP_7-synthesizing enzyme (Saiardi et al, 1999; Schell et al, 1999), the role of IP6K2 in the GIT has not been investigated until now. In this study, we observed that IP6K2 is prominently expressed in myenteric plexus (Fig. 4A-C), and genetic deletion of *IP6K2* diminishes IP_7 metabolism in the proximal GIT (Fig. 5F) as well as its muscularis externa containing myenteric plexus (Fig. 6J), suggesting the presence of an active IP6K2-IP_7 pathway in the ENS of the proximal GIT. Our

411 RNA-seq analysis of the duodenal muscularis externa indicated that genetic ablation of
412 *IP6K2* causes certain gene products associated with mature neurons to accumulate
413 concomitantly with the reduction of those of neural progenitor/stem cells and glial cells
414 (Fig. 7C and D). Given that the developmental lineage of enteric neurons comprises
415 several differentiation points such as neural crest cell migration, neuron-glia bifurcation,
416 and neural stem/progenitor cell differentiation into mature enteric neurons (Rao and
417 Gershon, 2018), inhibition of the IP6K2-IP_7 axis possibly causes developmental
418 imbalances of the ENS at the several differentiation points at least including the
419 maturation of both enteric neurons and glial cells. This idea is also supported by our
420 findings that IP6K2 inhibition significantly altered the expression levels of several
421 transcription factors regulating neural crest cell differentiation (Fig. 7E and F)
422 (Knoepfler et al, 2002; Vitelli et al, 2002; Abdelkhalek et al, 2004; Bussen et al, 2004;
423 Basch et al, 2006; Simões-Costa et al, 2012). In fact, IP6K2 activity was shown to be
424 required for normal migration and development of neural crest cells in zebrafish
425 (Sarmah and Wente, 2010). Besides, genetic inhibition of *IP6K2* in the duodenal
426 muscularis externa significantly or prominently changed mRNA levels of several genes
427 modulating neuronal functions (Fig. 7E, F and G). Notably, *Nckipsd* transcript, one of
428 the transcripts most significantly induced in *IP6K2*$^{-/-}$ duodenal muscularis externa,
429 contributes to the formation of neural dendrites (Fukuoka et al, 2001; Lee et al, 2006)
430 and intracellular neuronal signaling (Kim et al, 2009). These pieces of knowledge lead
431 to the hypothesis that the IP6K2-IP_7 axis might directly or indirectly contribute to
432 development and several distinct neuronal functions of enteric neurons, even though the
433 axis does not largely affect the entire morphological output of the ENS (Fig. 6E and F).
434 Future studies are required for elucidating how these differentially-expressed transcripts

435 controlled by the IP6K2-IP_7 axis individually affect ENS development and functioning.
436 Developmental and functional ENS defects often result in fatal congenital disorders
437 (Furness, 2012; Wright et al, 2021), but *IP6K2*$^{-/-}$ mice do not show such severe
438 phenotypic defects: *IP6K2*$^{-/-}$ mice are born at Mendelian ratio and grow normally,
439 similar to WT mice (Rao et al, 2014). Thus, the IP6K2-IP_7 axis might serve as a
440 fine-tuning factor for the developmental and functional regulation of the ENS, although
441 we could not exclude the possibility that *IP6K1*, another major IP6K isoform,
442 compensates for the loss of *IP6K2*. It will be meaningful to see whether ENS-specific
443 inhibition of IP6K2 and/or IP6K1 influences gastrointestinal pathophysiologies and
444 development of CNS diseases. Taken together, our observations provide valuable
445 insights into the field of PP-IP biology and neurogastroenterology.

446 Since dysregulation of IP_7 metabolism links to various human diseases including
447 neurodegenerative diseases, studying IP_7 metabolism in human organs provides
448 essential knowledge from the clinical point of view. The refined HILIC-MS/MS
449 protocol we described in this study is capable of detecting IP_6 and IP_7 not only in rodent
450 organs but also in human postmortem organs dissected after forensic intervention (Fig.
451 S5). Unlike in rodents, IP_7 level and IP_7/IP_6 ratio in the human proximal GITs
452 (esophagus, greater curvature and lesser curvature of the stomach) were less abundant
453 compared with those in human CNS. This is probably due to the high turnover rate of
454 PP-IPs and the delay in dissecting human postmortem organs. Forensic intervention and
455 subsequent organ dissection take hours after death The presence of the intestinal flora
456 may also facilitate the decomposition of these molecules in the GITs (Musshoff et al,
457 2011). Thus, care should be taken to assess IP_7 metabolism in human GITs. Although
458 the refined HILIC-MS/MS protocol can detect both IP_7 and IP_8, this protocol failed to

detect endogenous IP_8 in all rodent and human organs examined in this study, even in mouse GIT where IP_7 was explicitly abundant. This fact suggested that mammalian-derived IP_8 is far less abundant than IP_7, and its quantitative evaluation requires sample pooling or a more sensitive analytical protocol such as CE-MS (Qiu et al, 2020). In any case, we demonstrated that our novel protocol was able to evaluate IP_7 metabolism in human organs. Therefore, we foresee the diagnostic potential of our new analytical technique for analyzing IP_6 and IP_7 levels in clinical biopsy.

In conclusion, we investigated the distribution of PP-IPs in mammalian organs using a refined HILIC-MS/MS protocol and demonstrated that IP6K2-dependent IP_7 metabolism was enhanced in the ENS of the proximal GIT. This finding was corroborated by the observation that impairment of IP6K2-dependent IP_7 metabolism significantly altered certain neurotranscriptome profiles involved in ENS development and functioning. Further studies are needed to dissect molecular mechanisms underlying IP6K2-IP_7 axis-mediated neurotranscriptional regulation in the ENS, the role of IP_7 in neurogastroenterology, and processes involving the gut-brain axis. We believe that these findings shed new light on the physiological significance of the mammalian PP-IP pathway as well as the regulatory mechanisms of ENS functioning, which might contribute to a better understanding of human diseases associated with altered PP-IP metabolism.

Acknowledgements

We greatly appreciate Prof. Solomon H. Snyder of Johns Hopkins University for providing *IP6K2*$^{-/-}$ mice, Prof. Kazunori Nakajima and Dr. Yuki Hirota of Keio University for fruitful discussion, and Prof. Shinji Hadano of Tokai University for providing organs of purified diet-fed Sprague–Dawley rats. We thank Mr. Shingo Utsuki of the Liaison Laboratory Research Promotion Center in Kumamoto University for technical support of RNA sequencing, and the following staff members of the Support Center for Medical Research and Education of Tokai University for technical assistance: Akemi Kamijo, Katsuko Naito, Sachie Tanaka, Sanae Ogiwara, and Kayoko Iwao for animal experiments; Chisa Okada and Yuka Kitamura for confocal microscopic observation; and Keiko Yokoyama and Sanae Isaki for preliminary microarray experiments and data analysis. We also thank Editage (www.editage.jp) for English language editing. This research was partly supported by a Medical Research Council grant MR/T028904/1 (to A.S.) and grants-in-aid numbers JP19K07851 and JP22K07379 (to E.N.) and JP20H01002 (to M.I.) for scientific research from Japan Society for the Promotion of Science.

Author contributions

Conceptualization, M.I.; Methodology, M.I.; Investigation, M.I., N.F., S.K., S.H., T.I., K.H.; Formal Analysis, M.T., K.K., D.K.; Resources, C.W., Y.K., H.J.J.; Writing – Original Draft, M.I.; Writing – Review & Editing, M.I., A.S., E.N.; Visualization, M.I.; Funding Acquisition, M.I., A.S., E.N.; Supervision, A.S., E.N.; Project Administration, E.N.

Competing interests

The authors declare no competing interests.

STAR Methods

Key resources table

Reagent or resource	Source	Identifier
Antibodies		
Rabbit polyclonal anti-IP6K1	Sigma-Aldrich	Cat# HPA040825 RRID: AB_10960426
Goat polyclonal anti-IP6K2 (4F10)	Santa Cruz Biotechnology	Cat# sc-130012 RRID: AB_2127544
Rabbit polyclonal anti-IP6K2	Abcam	Cat# ab179921
Mouse monoclonal anti-β-actin (clone AC-15)	Sigma-Aldrich	Cat# A5441 RRID: AB_476744
Mouse monoclonal anti-HuC/D (clone 16A11)	Thermo Fisher Scientific	Cat# A-21271 RRID: AB_221448
Mouse monoclonal anti-βIII-tubulin (clone TUJ1)	Biolegend	Cat# 801201 RRID: AB_2313773
Rabbit immunoglobulin fraction (solid-phase absorbed)	Dako	Cat# X0936
Mouse IgG2a (isotype control)	R&D systems	Cat# MAB003
Mouse IgG2b (isotype control)	Dako	Cat# X0944
F(ab')2-Goat anti-Mouse IgG (H+L) Cross-Adsorbed Secondary Antibody, Alexa Fluor 594	Thermo Fisher Scientific	Cat# A-11020 RRID: AB_2534087

F(ab')2-Goat anti-Rabbit IgG (H+L) Cross-Adsorbed Secondary Antibody, Alexa Fluor 488	Thermo Fisher Scientific	Cat# A-11070 RRID: AB_2534114
Target Retrieval Solution	Dako	Cat# S1699
Chemicals, peptides, and recombinant proteins		
LC-MS grade acetonitrile	Honeywell	Cat# 349672.5
LC-MS grade ammonium bicarbonate	Honeywell	Cat# 40867-50G
Ultrapure water Ultrapure–grade ammonium hydroxide	Wako Pure Chemical Kanto Chemical	Cat# 210-01303 Cat# 01266-3B
InfinityLab deactivator additive	Agilent Technologies	Cat# 5191-3940
Inositol hexakisphosphate (IP_6)	Sigma-Aldrich	Cat# 68388
Sodium fluoride (NaF)	Sigma-Aldrich	Cat# S7920
Hexadeutero-myo-inositol trispyrophosphate (ITPP-d_6)	Toronto Research Chemical	Cat# I666022
Diphosphoinositol pentakisphosphate (IP_7)	This manuscript	N/A
Bisdiphosphoinositol tetrakisphosphate (IP_8)	This manuscript	N/A
HILICpak VG50 2D analytical column	Shodex	Cat# F7630300
HILICpak VG50G 2A guard column	Shodex	Cat# F6711200
Titansphere TiO_2 bead	GL Science	Cat# 5020-75000
Standard diet: CE-2	Clea Japan	https://www.clea-japan.com/
Purified diet: iVid-neo	Oriental Kobo	https://www.oyc.co.jp/en/
Purified diet: 70% casein	Clea Japan	https://www.clea-japan.com/

TRIzol reagent	Thermo Fisher Scientific	Cat# 15596026
TruSeq Stranded mRNA Kit	Illumina	Cat# 20020594
KAPA SYBR Fast qPCR kit	Kapa Biosystems	Cat# KK4602
Immobilon Western Chemiluminescent HRP Substrate	Millipore	Cat# WBKLS0500
Deposited data		
Human embryonic intestinal cell scRNA-seq datasets Mouse embryonic enteric nerve cell scRNA-seq datasets	Fawkner-Corbett et al, (2021) Morarach et al, (2021)	Human Fetal Gut Atlas (https://simmonslab.shinyapps.io/FetalAtlasDataPortal/) GEO: GSE149524
Mouse embryonic intestinal epithelial cell scRNA-seq datasets	Haber et al, (2017)	GEO: GSE92332
RNA-seq data	This manuscript	DDBJ: DRA014733
Experimental models: Cell lines		
HCT116	RIKEN	RCB2979 RRID: CVCL_0291
Experimental models: Organisms/strains		
Mouse: C57BL/6J	Clea Japan	C57BL/6JJcl
Mouse: *IP6K2*$^{-/-}$ (B6;129S-Ip6k2^{tm1Snyd}/J)	Laboratory of Solomon H. Snyder, Jackson Laboratory	Rao et al, (2014) Stock# 036426 RRID: IMSR_JAX:036426
Rat: Sprague-Dawley	Clea Japan	Jcl:SD
Oligonucleotides		
Primers for qPCR: please see Table S3	This manuscript	N/A
Software and algorithms		

LCMS solution (version 5.99)	Shimadzu	https://www.shimadzu.com
Seurat R package version 4.0.0	Butler et al, 2018	http://satijalab.org/seurat/ RRID: SCR_007322
Trim Galore (version 0.6.7)	Babraham institute	https://www.bioinformatics.babraham.ac.uk/projects/trim_galore/
HISAT2 (version 2.1.1)	Kim et al, 2019	https://github.com/DaehwanKimLab/hisat2
MarkDuplicates module of the Picard package	Broad Institute	http://broadinstitute.github.io/picard/
TPMCalculator (version 0.0.3)	Vera Alvarez et al, 2019	https://github.com/ncbi/TPMCalculator
EdgeR module of the TCC software (version 1.30.0)	Sun et al, 2013	http://bioconductor.org/
The Molecular Signatures Database (version 7.5.1)	Liberzon et al, 2015	http://www.gsea-msigdb.org/gsea/msigdb/index.jsp
DAVID Gene Ontology Analysis (version 6.8)	Huang da et al, 2009	http://david.abcc.ncifcrf.gov/ RRID: SCR_001881
Other		
LCMS-8050 mass spectrometer	Shimadzu	https://www.shimadzu.com
NextSeq500 sequencer	Illumina	https://www.illumina.com/
LSM 880 microscope	Carl Zeiss	https://www.zeiss.com/
EzCapture MZ chemiluminescent detector	ATTO	https://www.attoeng.site/
StepOne Plus Real-Time PCR system	Applied Biosystems	https://www.thermofisher.com/
4150 TapeStation System	Agilent Technologies	https://www.agilent.com
NanoDrop 8000 spectrophotometer	Thermo Fisher Scientific	https://www.thermofisher.com/

RESOURCE AVAILABILITY

Lead contact

Further information and requests for resources and reagents should be directed to and will be fulfilled by the Lead Contact, Eiichiro Nagata (enagata@is.icc.u-tokai.ac.jp) or Masatoshi Ito (masa104-ito@tokai-u.jp).

Materials availability

Requests for materials generated in this study should be directed to the Lead Contact. The availability of these materials may be limited because their chemical synthesis requires multiple laborious and costly processes.

Data and code availability

The raw RNA-seq data have been deposited at the DNA Data Bank of Japan (DDBJ) and are publicly available as of the date of publication (accession number DRA014733). Raw GSEA data shown in Fig. 7C are available in the Data S1 file. Other individual datasets and corresponding files generated in this study are available upon reasonable request from the Lead Contact.

EXPERIMENTAL MODEL AND SUBJECT DETAILS

Cell culture

HCT116 cells were cultured in DMEM (Nacalai Tesque, Kyoto, Japan) supplemented with 10% FBS in 5% CO_2. Cells prepared at 60% confluence in 10 cm dishes were incubated for 1 h with or without 50 mM sodium fluoride (Sigma-Aldrich, St. Louis, MO, USA). After washing twice with PBS, the cells were lysed in cell lysis buffer (0.01% Triton X-100, 1 mM EDTA, 20 mM Tris-HCl). A small aliquot was set aside for protein quantitation, and the rest was used for purification of IPs.

535 **Mouse organs**

536 All experiments involving animals were performed in accordance with protocols
537 approved by institutional animal care guidelines (Tokai University School of Medicine).
538 Male C57 BL/6J mice and Sprague–Dawley rats obtained from Clea Japan (Tokyo,
539 Japan) were maintained on a standard diet (CE-2; Clea Japan) or purified diet (iVid-neo;
540 Oriental Kobo, 70% casein; Clea Japan). Some mice fed a standard diet or purified diet
541 were fasted for 48 h before sacrifice. *IP6K2*$^{-/-}$ and WT mice maintained on a standard
542 diet were switched to the purified diet for a week and subsequently fasted for 48 h
543 before sacrifice. During fasting, mouse cages were changed to clean ones with new
544 bedding every 24 h to reduce coprophagy. Mice and rats were anesthetized using
545 isoflurane and then sacrificed by whole blood withdrawal from the left atrium. Before
546 dissection of the organs, the animals were perfused transcardially with ice-cold PBS to
547 wash out the residual blood and prevent the detection of IPs derived from blood cells.
548 GIT organs (stomach, duodenum, small intestine, and colon) were cut open to remove
549 feces and then extensively rinsed with PBS to wash out any dietary residuals. The
550 duodenum, small intestine, and colon were harvested by cutting a 5 cm (mouse) or 10
551 cm (rat) segment from the distal end of stomach, between 10 and 15 cm (mouse) or 20
552 and 30 cm (rat) away from the duodenum and from the anus, respectively. The
553 harvested organs were frozen until further use.

554

555 **Isolation of muscularis externa from mouse GITs**

556 The muscularis externa containing myenteric plexuses was prepared from mouse
557 GITs as previously described with some modification (Fujita et al, 2018; Ahrends et al,
558 2022). For HILIC-MS/MS, mouse GIT segments were cut open along the attachment

559 line of the mesentery and then placed onto a cold surface with the muscularis externa
560 facing up. The muscularis externa of the GIT segments was isolated by gently scraping
561 the outer layer with watchmaker tweezers under a binocular stereomicroscope. For
562 whole-mount immunostaining, the mouse duodenum was cut open along the mesentery
563 line, pinned onto a rubber plate, and then fixed with 4% paraformaldehyde (PFA)
564 overnight at 4 °C. The muscularis layer was then gently separated from the GIT
565 segment using watchmaker tweezers and a cotton swab under a binocular
566 stereomicroscope. For RNA extraction, mouse GITs were immersed in saturated
567 ammonium sulfate solution containing 20 mM EDTA and 25 mM sodium citrate
568 (pH5.2) to inhibit RNA degradation. The muscularis externa of the segments was placed
569 over a glass rod and then peeled away using a cotton swab along the attachment line of
570 the mesentery under a binocular stereomicroscope as described previously (Smith et al,
571 2013). Isolated muscularis externa was stored in saturated ammonium sulfate solution
572 and then frozen until further use.
573
574 **Human postmortem organs**
575 The human study was approved by the Ethics Committee of Tokai University
576 (institutional review board number: 20I-02), and the study protocol conformed to the
577 ethical guidelines of the 1975 Declaration of Helsinki (World Medical Association,
578 2013). Written informed consent, allowing the experimental use of the organ samples,
579 was obtained from the relatives of all subjects. Human postmortem organs were
580 obtained at autopsies from three donated bodies (two men and one woman; mean age,
581 62.3 ± 22.8 years; average body mass index, 26.4 ± 6.6). Some anomalies, such as
582 cardiac hypertrophy, were observed in their bodies by a forensic pathologist. To

minimize organ decomposition, organ sampling was confined to cases where the death date and ambient temperature were explicit and the accumulated degree–days [ADD; environmental temperature (°C) × postmortem interval (day)] value—an index for evaluating the quality of forensic samples (Pittner *et al*, 2016)—of all three bodies were very low (close to or less than 20). The harvested organ samples (approximately 400 mg) were frozen until further use.

METHOD DETAILS

Gel electrophoresis of synthetic PP-IPs

IP_7 and IP_8 were synthesized from myo-inositol using fluorenylmethyl phosphoramidite chemistry as described previously (Pavlovic et al, 2016). The synthetic PP-IPs were validated using polyacrylamide gel electrophoresis as previously described (Losito et al, 2009). Briefly, synthetic PP-IPs samples mixed with orange G and bromophenol blue loading buffer were applied onto 35% polyacrylamide/Tris-borate-EDTA gel. The samples were electrophoresed overnight at 4 °C at 600 V and 6 mA until the orange G and bromophenol blue had run through two-thirds of the gel. Gels were stained with toluidine blue and scanned using a computer scanner.

Purification of IPs

IPs in biological samples were purified as described previously (Wilson et al, 2015), with some modification. Frozen organs, diets, and feces samples were homogenized using a Shake Master Neo (Bio Medical Science, Tokyo, Japan) in 500 µL of ultrapure water. Feces samples were air-dried overnight before homogenization for accurate comparison of IP_6 and IP_7 concentrations with those in the diet. Crude lysate was mixed

with an equal volume of 2 M perchloric acid (PCA), incubated on ice for 30 min, and centrifuged to remove tissue debris. After spiking with 3 nmol of ITPP-d_6 as an internal control, 5 mg of TiO_2 beads (GL Sciences, Tokyo, Japan) were added to each sample. The beads were incubated at 4 °C for 30 min and washed twice with 1 M PCA, and then 200 µL of 10% ammonium hydroxide was added for IP elution. The elution step was repeated to maximize recovery. The total eluate was dried using a SpeedVac concentrator (Thermo Fisher Scientific, Waltham, MA, USA) and reconstituted in 125 µL of 100 mM ammonium carbonate/40% acetonitrile buffer, 50 µL of which was used for LC-MS.

HILIC-MS/MS analysis for PP-IPs

Chromatographic experiments were performed using a Nexera UHPLC instrument (Shimadzu, Kyoto, Japan). HILIC-based chromatographic separation of IP_6, IP_7, IP_8, and the internal control ITPP-d_6 was achieved using a modified version of a previously described procedure (Ito et al, 2018). The mobile phase was composed of 300 mM ammonium bicarbonate buffer (pH 10.5) containing 0.1% InfinityLab deactivator additive (Agilent Technologies) as the aqueous mobile phase (eluent A), and 90% acetonitrile containing 10 mM ammonium bicarbonate buffer (pH 10.5) and 0.1% InfinityLab deactivator additive as the organic mobile phase (eluent B). Eluent B included more than 10% aqueous solvent to prevent polymeric aggregation of the major constituent (medronic acid) in the additive. In the entire LC system, chromatographic stainless steel tube was treated with 0.5% phosphoric acid in 90% acetonitrile overnight before analysis to block undesirable adsorption of analytes on the surface of the inner wall of the tube, while paying attention not to run the solvent into the mass spectrometer.

The total flow rate of the mobile phase was 0.4 mL/min. Linear gradient separation was achieved as follows: 0–2 min, 75% B; 2–12 min, 75%–2% B; 12–15 min, 2% B.

RNA extraction and quantitative PCR analysis

GIT segments and their muscularis externa were carefully collected and subjected to RNA extraction, as previously described (Augereau et al, 2016). Total RNA was extracted using TRIzol reagent (Invitrogen, Carlsbad, CA, USA). RNA concentration and quality were determined using a NanoDrop 8000 spectrophotometer (Thermo Fisher Scientific) and the 4150 TapeStation system (Agilent Technologies), respectively. Complementary DNA was generated using the High-Capacity Reverse Transcription Kit (Applied Biosystems). qPCR was performed using the KAPA SYBR Fast qPCR kit (Kapa Biosystems, Wilmington, MA, USA) and a StepOne Plus Real-Time PCR system (Applied Biosystems, Foster City, CA, USA). The primer sequences used in this study are listed in Table S3.

RNA sequencing

Total RNA samples of WT and *IP6K2*-deficient duodenal muscle externa with around 7.0 of RNA integrity number were subjected to RNA-seq analysis. RNA sequencing libraries were prepared using TruSeq Stranded mRNA Kit (Illumina, San Diego, CA, USA) according to the manufacturer's instructions. Each library was sequenced in 1 × 75 bp of single read mode using a NextSeq 500 platform (Illumina). Adapter sequences are removed from sequencing reads using Trim Galore (version 0.6.7; https://www.bioinformatics.babraham.ac.uk/projects/trim_galore/). Sequence reads were aligned to mouse genome (mm10) by HISAT2 (version 2.1.1) (Kim et al, 2018).

Duplicate reads were removed using the MarkDuplicates module of the Picard package (version 2.27.3; http://broadinstitute.github.io/picard/). The following genes were excluded before processing for the expression data analysis: highly expressing mucosal digestive enzyme genes (*Amy2a1*, *Amy2a2*, *Amy2a3*, *Amy2a4*, *Amy2a5*, *Amy2b*, *Amy1*, *Try4*, *Try5*, *Try10*) contaminated during the muscularis isolation, mitochondrial genes, and long non-coding RNAs. Expression levels of genes annotated in GENCODE (version M25) were quantitated by TPMCalculator (version 0.0.3) (Vera Alvarez et al, 2019). The software described above was run with the default parameters. Differentially expressed genes were identified by the EdgeR module of the TCC software (version 1.30.0) (Sun et al, 2013). GSEA was performed as described previously (Subramanian et al, 2005). Gene sets used in this study were retrieved from The Molecular Signatures Database (version 7.5.1; http://www.gsea-msigdb.org/gsea/msigdb/index.jsp) (Liberzon et al, 2015). Pathway enrichment analysis was performed using the online database DAVID (http://david.abcc.ncifcrf.gov) (Huang da et al, 2009).

Western blot analysis

Western blot analysis was performed as previously described (Nagata et al, 2011). Membranes were incubated with anti-IP6K1 (Sigma-Aldrich), anti-IP6K2 (Santa Cruz Biotechnology, Dallas, TX, USA) and anti-β-actin (Sigma-Aldrich) primary antibodies overnight at 4□°C. After rinsing 3 times in PBS containing 0.05% Tween-20, the membranes were incubated with the appropriate secondary antibodies conjugated with horseradish peroxidase (HRP) (donkey anti-rabbit IgG, HRP-linked F(ab')$_2$ fragment or sheep anti-mouse IgG, HRP-linked F(ab')$_2$ fragment; GE Healthcare, Buckinghamshire, UK). The immunoreactivities of the primary antibodies were visualized with Immobilon

679 Western Chemiluminescent HRP Substrate (Millipore, Billerica, MA, USA) and
680 recorded using an Ez-Capture Analyzer (ATTO, Tokyo, Japan).
681
682 **Immunohistochemistry**
683 Preparation of formalin-fixed, paraffin-embedded (FFPE) sections was described
684 previously (Nagata et al, 2016). After deparaffinization and rehydration, the mouse
685 tissue sections were incubated with Target Retrieval Solution (Dako, Glostrup,
686 Denmark) at 98 °C for 10 min. Thereafter, the sections were washed thrice with 0.05%
687 Tween-20 in Tris-buffered saline (TBS), blocked using 5% normal goat serum for 15
688 min, and then incubated with primary antibodies against IP6K2 (1:100, ab179921,
689 Abcam, Cambridge, MA, USA) or HuC/D (1:100, A-21271, Thermo Fisher Scientific)
690 overnight at 4□°C. Rabbit immunoglobulin (Dako) and mouse IgG2b isotype control
691 (Dako) were used to evaluate non-specific binding. After rinsing thrice with 0.05%
692 Tween-20 in TBS, the sections were incubated with secondary goat anti-rabbit IgG
693 Alexa 488 (1:350, A-11070, Thermo Fisher Scientific) and goat anti-mouse IgG Alexa
694 594 (1:350, A-11020, Thermo Fisher Scientific) antibodies for 30 min at room
695 temperature. The sections were then washed thrice with 0.05% Tween-20 in TBS and
696 mounted using anti-fading medium (12.5 mg/mL DABCO, 90% glycerol, pH 8.8 in
697 PBS). Confocal fluorescence images were obtained using a LSM 880 microscope (Carl
698 Zeiss, Jena, Germany).
699
700 **Whole-mount immunostaining**
701 Immunostaining of duodenal muscularis externa was performed as previously described
702 with minor modifications (Fujita et al, 2018; Ahrends et al, 2022). Briefly, duodenal

703 muscularis externa isolated from WT and *IP6K2*$^{-/-}$ mice were blocked with 3% BSA
704 blocking solution containing the corresponding isotype control antibodies for 2 days
705 after fixation with 4% PFA overnight. The muscle layers were then washed with PBS
706 containing 0.05% Triton X-100 and incubated with diluted primary antibodies against
707 HuC/D (Thermo Fisher Scientific) or βIII-Tubulin (Biolegend, San Diego, CA, USA)
708 for 3 days. After rinsing thrice with 0.05% Triton X-100 in PBS, the muscularis externa
709 were then incubated with secondary goat anti-mouse IgG Alexa 594 (1:350, A-11020,
710 Thermo Fisher Scientific) for 3 h at room temperature. The samples were then washed
711 thrice with 0.05% Triton X-100 in PBS and mounted using anti-fading medium (12.5
712 mg/mL DABCO, 90% glycerol, pH 8.8 in PBS). Fluorescence images were obtained
713 using a LSM 880 confocal microscope (Carl Zeiss).
714
715 **Computational analysis of scRNA-seq datasets**
716 Publicly available human embryonic intestine scRNA-seq processed data
717 (Fawkner-Corbett et al, 2021) and mouse embryonic ENS matrix data (Morarach et al,
718 2021) were downloaded from the Human Fetal Gut Atlas
719 (https://simmonslab.shinyapps.io/FetalAtlasDataPortal/) and the GEO database
720 (identifier: GSE149524), respectively. Mouse embryonic intestinal epithelial cell data
721 (Haber et al, 2017) were obtained from the GEO database (identifier: GSE92332). The
722 above datasets were analyzed using the R package Seurat version 4.0.0 (Butler et al,
723 2018) to perform dimensionality reduction by uniform manifold approximation and
724 projection and/or generate dot plots showing the relative expression of IP6Ks across
725 different clusters.
726

QUANTIFICATION AND STATISTICAL ANALYSIS

Data are expressed as the mean ± SD. Differences between two or more groups were analyzed using two-tailed Student's *t*-test or one-way analysis of variance (ANOVA) followed by Bonferroni-type post-hoc test, respectively. In RNA-seq analyses, P values were determined using the corresponding analytical tools. Statistical significance was set at $P < 0.05$.

References

1. Abdelkhalek HB, Beckers A, Schuster-Gossler K, Pavlova MN, Burkhardt H, Lickert H, Rossant J, Reinhardt R, Schalkwyk LC, Müller I, et al. (2004) The mouse homeobox gene Not is required for caudal notochord development and affected by the truncate mutation. *Genes & Dev*. 18: 1725-1736 [10.1101/gad.303504]
2. Ahrends T, Weiner M, and Mucida D (2022) Isolation of myenteric and submucosal plexus from mouse gastrointestinal tract and subsequent flow cytometry and immunofluorescence. *STAR Protoc*. 3: 101157 [10.1016/j.xpro.2022.101157].
3. Augereau C, Lemaigre FP, and Jacquemin P (2016) Extraction of high-quality RNA from pancreatic tissues for gene expression studies. *Anal. Biochem*. 500: 60-62 [10.1016/j.ab.2016.02.008].
4. Azevedo C, and Saiardi A (2006) Extraction and analysis of soluble inositol polyphosphates from yeast. *Nat. Protoc*. 1: 2416-2422 [10.1038/nprot.2006.337].
5. Basch M, Bronner-Fraser M, and García-Castro MI (2006) Specification of the neural crest occurs during gastrulation and requires Pax7. *Nature* 441: 218-222 [10.1038/nature04684]
6. Bussen M, Petry M, Schuster-Gossler K, Leitges M, Gossler A, and Kispert A (2004) The T-box transcription factor Tbx18 maintains the separation of anterior and posterior somite compartments. *Genes & Dev*. 18: 1209-1221 [10.1101/gad.300104]
7. Butler A, Hoffman P, Smibert P, Papalexi E, and Satija R (2018) Integrating single-cell transcriptomic data across different conditions, technologies, and species. *Nat. Biotechnol*. 36: 411-420 [10.1038/nbt.4096].

759 8. Cao J, O'Day DR, Pliner HA, Kingsley PD, Deng M, Daza RM, Zager MA,
760 Aldinger KA, Blecher-Gonen R, Zhang F, et al. (2020) A human cell atlas of fetal
761 gene expression. *Science* 370: eaba7721 [10.1126/science.aba7721]
762 9. Chakraborty A (2018) The inositol pyrophosphate pathway in health and diseases.
763 *Biol. Rev. Camb. Philos. Soc*. 93: 1203-1227 [10.1111/brv.12392].
764 10. Chakraborty A, Koldobskiy MA, Bello NT, Maxwell M, Potter JJ, Juluri KR,
765 Maag D, Kim S, Huang AS, Dailey MJ, et al. (2010) Inositol pyrophosphates
766 inhibit Akt signaling, thereby regulating insulin sensitivity and weight gain. *Cell*
767 143: 897-910 [10.1016/j.cell.2010.11.032].
768 11. Crocco P, Saiardi A, Wilson MS, Maletta R, Bruni AC, Passarino G, and Rose G
769 (2016) Contribution of polymorphic variation of inositol hexakisphosphate kinase
770 3 (IP6K3) gene promoter to the susceptibility to late onset Alzheimer's disease.
771 *Biochim. Biophys. Acta* 1862: 1766-1773 [10.1016/j.bbadis.2016.06.014].
772 12. Draskovic P, Saiardi A, Bhandari R, Burton A, Ilc G, Kovacevic M, Snyder SH,
773 and Podobnik M (2008) Inositol hexakisphosphate kinase products contain
774 diphosphate and triphosphate groups. *Chem. Biol*. 15: 274-286
775 [10.1016/j.chembiol.2008.01.011].
776 13. Dong J, Ma G, Sui L, Wei M, Satheesh V, Zhang R, Ge S, Li J, Zhang TE, Wittwer
777 C, et al. (2019) Inositol Pyrophosphate InsP8 Acts as an Intracellular Phosphate
778 Signal in Arabidopsis. *Mol. Plant*. 12: 1463-1473 [10.1016/j.molp.2019.08.002].
779 14. Dorsch JA, Cook A, Young K, Anderson JM, Bauman AT, Volkmann CJ, Murthy
780 PPN, and Raboy V (2003) Seed phosphorus and inositol phosphate phenotype of
781 barley low phytic acid genotypes. *Phytochemistry* 62: 691-706
782 [10.1016/s0031-9422(02)00610-6].

15. Duong QH, Clark KD, Lapsley KG, and Pegg RB (2017) Quantification of inositol phosphates in almond meal and almond brown skins by HPLC/ESI/MS. *Food Chem*. 229: 84-92 [10.1016/j.foodchem.2017.02.031].

16. Eiseman J, Lan J, Guo J, Joseph E, and Vucenik I (2011) Pharmacokinetics and tissue distribution of inositol hexaphosphate in C.B17 SCID mice bearing human breast cancer xenografts. *Metabolism* 60: 1465-1474 [10.1016/j.metabol.2011.02.015].

17. Everaert C, Luypaert M, Maag JLV, Cheng QX, Dinger ME, Hellemans J, and Mestdagh P (2017) Benchmarking of RNA-sequencing analysis workflows using whole-transcriptome RT-qPCR expression data. *Sci. Rep.* 7: 1559 [10.1038/s41598-017-01617-3]

18. Fan X, Dong J, Zhong S, Wei Y, Wu Q, Yan L, Yong J, Sun L, Wang X, Zhao Y, et al. (2018) Spatial transcriptomic survey of human embryonic cerebral cortex by single-cell RNA-seq analysis. *Cell Res*. 28: 730-745 [10.1038/s41422-018-0053-3]

19. Fawkner-Corbett D, Antanaviciute A, Parikh K, Jagielowicz M, Gerós AS, Gupta T, Ashley N, Khamis D, Fowler D, Morrissey E, et al. (2021) Spatiotemporal analysis of human intestinal development at single-cell resolution. *Cell* 184: 810-826.e23 [10.1016/j.cell.2020.12.016].

20. Fu C, Xu J, Cheng W, Rojas T, Chin AC, Snowman AM, Harraz MM, and Snyder SH (2017) Neuronal migration is mediated by inositol hexakisphosphate kinase 1 via alpha-actinin and focal adhesion kinase. *Proc. Natl. Acad. Sci. U. S. A.* 114: 2036-2041 [10.1073/pnas.1700165114].

21. Fujita M, Yagi T, Okura U, Tanaka J, Hirashima N, and Tanaka M (2018)

807 Calcineurin B1 deficiency in glial cells induces mucosal degeneration and
808 inflammation in mouse small intestine. *Biol. Pharm. Bull*. 41: 786-796.
809 [10.1248/bpb.b18-00041]
810 22. Fukuoka M, Suetsugu S, Miki H, Fukami K, Endo T, and Takenawa T (2001) A
811 novel neural Wiskott-Aldrich syndrome protein (N-WASP) binding protein, WISH,
812 induces Arp2/3 complex activation independent of Cdc42. *J. Cell Biol*. 152:
813 471-482 [10.1083/jcb.152.3.471]
814 23. Furness JB (2012) The enteric nervous system and neurogastroenterology. *Nat.*
815 *Rev. Gastroenterol. Hepatol*. 9: 286-294 [10.1038/nrgastro.2012.32]
816 24. Ghoshal S, Zhu Q, Asteian A, Lin H, Xu H, Ernst G, Barrow JC, Xu B, Cameron
817 MD, Kamenecka TM, et al. (2016) TNP [N2-(m-Trifluorobenzyl),
818 N6-(p-nitrobenzyl)purine] ameliorates diet induced obesity and insulin resistance
819 via inhibition of the IP6K1 pathway. *Mol. Metab*. 5: 903-917
820 [10.1016/j.molmet.2016.08.008].
821 25. Gremel G, Wanders A, Cedernaes J, Fagerberg L, Hallström B, Edlund K, Sjöstedt
822 E, Uhlén M, and Pontén F (2015) The human gastrointestinal tract-specific
823 transcriptome and proteome as defined by RNA sequencing and antibody-based
824 profiling. *J. Gastroenterol*. 50: 46-57 [10.1007/s00535-014-0958-7].
825 26. Gu C, Liu J, Liu X, Zhang H, Luo J, Wang H, Locasale JW, and Shears SB (2021)
826 Metabolic supervision by PPIP5K, an inositol pyrophosphate kinase/phosphatase,
827 controls proliferation of the HCT116 tumor cell line. *Proc. Natl. Acad. Sci. U. S. A.*
828 118: e2020187118 [10.1073/pnas.2020187118].
829 27. Haber AL, Biton M, Rogel N, Herbst RH, Shekhar K, Smillie C, Burgin G,
830 Delorey TM, Howitt MR, Katz Y, et al. (2017) A single-cell survey of the small

intestinal epithelium. *Nature* 551: 333-339 [10.1038/nature24489].

28. Hsiao JJ, Potter OG, Chu TW, and Yin H (2018) Improved LC/MS Methods for the Analysis of Metal-Sensitive Analytes Using Medronic Acid as a Mobile Phase Additive. *Anal. Chem*. 90: 9457-9464 [10.1021/acs.analchem.8b02100].

29. Huang da W, Sherman BT, and Lempicki RA (2009) Systematic and integrative analysis of large gene lists using DAVID bioinformatics resources. *Nat. Protoc*. 4: 44-57 [10.1038/nprot.2008.211].

30. Irvine RF, and Schell MJ (2001) Back in the water: the return of the inositol phosphates. *Nat. Rev. Mol. Cell Biol*. 2: 327-338 [10.1038/35073015].

31. Ito M, Fujii N, Wittwer C, Sasaki A, Tanaka M, Bittner T, Jessen HJ, Saiardi A, Takizawa S, and Nagata E (2018) Hydrophilic interaction liquid chromatography-tandem mass spectrometry for the quantitative analysis of mammalian-derived inositol poly/pyrophosphates. *J. Chromatogr. A* 1573: 87-97 [10.1016/j.chroma.2018.08.061].

32. Kim D, Paggi JM, Park C, Bennett C, and Salzberg SL (2018) Graph-based genome alignment and genotyping with HISAT2 and HISAT-genotype. *Nat. Biotech*. 37: 907-915 [10.1038/s41587-019-0201-4]

33. Kim SM, Choi KY, Cho IH, Rhy JH, Kim SH, Park CS, Kim E, and Song WK (2009) Regulation of dendritic spine morphology by SPIN90, a novel Shank binding partner. *J. Neurochem*. 109: 1106-1117 [10.1111/j.1471-4159.2009.06039.x]

34. Knoepfler PS, Cheng PF, and Eisenman RN (2002) N-myc is essential during neurogenesis for the rapid expansion of progenitor cell populations and the inhibition of neuronal differentiation. *Genes & Dev*. 16: 2699-2712

[10.1101/gad.1021202]

35. Kolozsvari B, Firth S, and Saiardi A (2015) Raman spectroscopy detection of phytic acid in plant seeds reveals the absence of inorganic polyphosphate. *Mol. Plant*. 8: 826-828 [10.1016/j.molp.2015.01.015].

36. Laha D, Portela-Torres P, Desfougères Y, and Saiardi A (2021) Inositol phosphate kinases in the eukaryote landscape. *Adv. Biol. Regul*. 79: 100782 [10.1016/j.jbior.2020.100782].

37. Lee S, Lee K, Hwang S, Kim SH, Song WK, Park ZY, and Chang S (2006) SPIN90/WISH interacts with PSD-95 and regulates dendritic spinogenesis via an N-WASP-independent mechanism. *EMBO J*. 25: 4983-4995 [10.1038/sj.emboj.7601349]

38. Li X, Gu C, Hostachy S, Sahu S, Wittwer C, Jessen HJ, Fiedler D, Wang H, and Shears SB (2020) Control of XPR1-dependent cellular phosphate efflux by InsP8 is an exemplar for functionally-exclusive inositol pyrophosphate signaling. *Proc. Natl. Acad. Sci. U. S. A.* 117: 3568-3574 [10.1073/pnas.1908830117].

39. Liberzon A, Birger C, Thorvaldsdóttir H, Ghandi M, Mesirov JP, and Tamayo P (2015) The Molecular Signatures Database (MSigDB) hallmark gene set collection. *Cell Syst*. 1: 417-425 [10.1016/j.cels.2015.12.004]

40. Liu X, Villalta PW, and Sturla SJ (2009) Simultaneous determination of inositol and inositol phosphates in complex biological matrices: quantitative ion-exchange chromatography/tandem mass spectrometry. *Rapid Commun. Mass Spectrom.* 23: 705-712 [10.1002/rcm.3923].

41. López-Sánchez U, Tury S, Nicolas G, Wilson MS, Jurici S, Ayrignac X, Courgnaud V, Saiardi A, Sitbon M, and Battini JL (2020) Interplay between

879 primary familial brain calcification-associated SLC20A2 and XPR1 phosphate
880 transporters requires inositol polyphosphates for control of cellular phosphate
881 homeostasis. *J. Biol. Chem*. 295: 9366-9378 [10.1074/jbc.RA119.011376].
882 42. Losito O, Szijgyarto Z, Resnick AC, and Saiardi A (2009) Inositol pyrophosphates
883 and their unique metabolic complexity: analysis by gel electrophoresis. *PLoS One*
884 4: e5580 [10.1371/journal.pone.0005580].
885 43. La Manno G, Gyllborg D, Codeluppi S, Nishimura K, Salto C, Zeisel A, Borm L,
886 Stott SRW, Toledo EM, Villaescusa JC, et al. (2016) Molecular diversity of
887 midbrain development in mouse, human, and stem cells. *Cell* 167: 566-580
888 [10.1016/j.cell.2016.09.027]
889 44. Menniti FS, Miller RN, Putney JW Jr, and Shears SB (1993) Turnover of inositol
890 polyphosphate pyrophosphates in pancreatoma cells. *J. Biol. Chem*. 268:
891 3850-3856 [10.1016/S0021-9258(18)53551-1].
892 45. Morarach K, Mikhailova A, Knoflach V, Memic F, Kumar R, Li W, Ernfors P, and
893 Marklund U (2021) Diversification of molecularly defined myenteric neuron
894 classes revealed by single-cell RNA sequencing. *Nat. Neurosci*. 24: 34-46
895 [10.1038/s41593-020-00736-x].
896 46. Moritoh Y, Oka M, Yasuhara Y, Hozumi H, Iwachidow K, Fuse H, and Tozawa R
897 (2016) Inositol Hexakisphosphate Kinase 3 Regulates Metabolism and Lifespan in
898 Mice. *Sci. Rep*. 6: 32072 [10.1038/srep32072].
899 47. Musshoff F, Klotzbach H, Block W, Traeber F, Schild H, and Madea B (2011)
900 Comparison of post-mortem metabolic changes in sheep brain tissue in isolated
901 heads and whole animals using 1H-MR spectroscopy--preliminary results. *Int. J.*
902 *Legal Med*. 125: 741-744 [10.1007/s00414-010-0463-3].

903 48. Nagata E, Nonaka T, Moriya Y, Fujii N, Okada Y, Tsukamoto H, Itoh J, Okada C,
904 Satoh T, Arai T, et al. (2016) Inositol Hexakisphosphate Kinase 2 Promotes Cell
905 Death in Cells with Cytoplasmic TDP-43 Aggregation. *Mol. Neurobiol*. 53:
906 5377-5383 [10.1007/s12035-015-9470-1].
907 49. Nagata E, Saiardi A, Tsukamoto H, Okada Y, Itoh Y, Satoh T, Itoh J, Margolis RL,
908 Takizawa S, Sawa A, et al. (2011) Inositol hexakisphosphate kinases induce cell
909 death in Huntington disease. *J. Biol. Chem.* 286: 26680-26686
910 [10.1074/jbc.M111.220749].
911 50. Nagpal L, Fu C, and Snyder SH (2018) Inositol Hexakisphosphate Kinase-2 in
912 Cerebellar Granule Cells Regulates Purkinje Cells and Motor Coordination via
913 Protein 4.1N. *J. Neurosci*. 38: 7409-7419 [10.1523/JNEUROSCI.1165-18.2018].
914 51. Nagpal L, Kornberg MD, Albacarys LK, and Snyder SH (2021) Inositol
915 hexakisphosphate kinase-2 determines cellular energy dynamics by regulating
916 creatine kinase-B. *Proc. Natl. Acad. Sci. U. S. A.* 118: e2020695118
917 [10.1073/pnas.2020695118].
918 52. Norbis F, Boll M, Stange G, Markovich D, Verrey F, Biber J, and Murer H (1997)
919 Identification of a cDNA/protein leading to an increased Pi-uptake in Xenopus
920 laevis oocytes. *J. Membr. Biol*. 156: 19-24 [10.1007/s002329900183].
921 53. Park SE, Lee D, Jeong JW, Lee SY, Park SJ, Ryu J, Oh SK, Yang H, Fang S, and
922 Kim S (2022) Gut epithelial inositol polyphosphate multikinase alleviates
923 experimental colitis via governing tuft cell homeostasis. *Cell Mol. Gastroenterol.*
924 *Hepatol*. S2352-345X(22)00182-5. [10.1016/j.jcmgh.2022.08.004]
925 54. Pavlovic I, Thakor DT, Vargas JR, McKinlay CJ, Hauke S, Anstaett P, Camuña RC,
926 Bigler L, Gasser G, Schultz C, et al. (2016) Cellular delivery and photochemical

release of a caged inositol-pyrophosphate induces PH-domain translocation in cellulo. *Nat. Commun*. 7: 10622 [10.1038/ncomms10622].

55. Pittner S, Ehrenfellner B, Monticelli FC, Zissler A, Sänger AM, Stoiber W, and Steinbacher P (2016) Postmortem muscle protein degradation in humans as a tool for PMI delimitation. *Int. J. Legal Med*. 130: 1547-1555 [10.1007/s00414-016-1349-9].

56. Priyodip P, Prakash PY, and Balaji S (2017) Phytases of Probiotic Bacteria: Characteristics and Beneficial Aspects. *Indian J. Microbiol*. 57: 148-154 [10.1007/s12088-017-0647-3].

57. Qiu D, Wilson MS, Eisenbeis VB, Harmel RK, Riemer E, Haas TM, Wittwer C, Jork N, Gu C, Shears SB, et al. (2020) Analysis of inositol phosphate metabolism by capillary electrophoresis electrospray ionization mass spectrometry. *Nat. Commun*. 11: 6035 [10.1038/s41467-020-19928-x].

58. Rao F, Cha J, Xu J, Hu R, Vandiver MS, Tyagi R, Tokhunts R, Koldobski MA, Fu C, Barrow R, et al. (2014) Inositol pyrophosphates mediate the DNA-PK/ATM-p53 cell death pathway by regulating CK2 phosphorylation of Tti1/Tel2. *Mol. Cell* 54: 119-132 [10.1016/j.molcel.2014.02.020].

59. Rao F, Xu J, Fu C, Cha JY, Gadalla MM, Xu R, Barrow JC, and Snyder SH (2015) Inositol pyrophosphates promote tumor growth and metastasis by antagonizing liver kinase B1. *Proc. Natl. Acad. Sci. U. S. A.* 112: 1773-1778 [10.1073/pnas.1424642112].

60. Rao M, and Gershon MD (2018) Enteric nervous system development: what could possibly go wrong? *Nat. Rev. Neurosci*. 19: 552-565. [10.1038/s41583-018-0041-0]

951 61. Ried MK, Wild R, Zhu J, Pipercevic J, Sturm K, Broger L, Harmel RK, Abriata
952 LA, Hothorn LA, Fiedler D, et al. (2021) Inositol pyrophosphates promote the
953 interaction of SPX domains with the coiled-coil motif of PHR transcription factors
954 to regulate plant phosphate homeostasis. *Nat. Commun*. 12: 384-020-20681-4
955 [10.1038/s41467-020-20681-4].
956 62. Riemer E, Qiu D, Laha D, Harmel RK, Gaugler P, Gaugler V, Frei M, Hajirezaei
957 MR, Laha NP, Krusenbaum L, et al. (2021) ITPK1 is an $InsP_6$/ADP
958 phosphotransferase that controls phosphate signaling in Arabidopsis. *Mol. Plant*.
959 14: 1864-1880 [10.1016/j.molp.2021.07.011].
960 63. Robert C, and Watson M (2015) Errors in RNA-Seq quantification affect genes of
961 relevance to human disease. *Genome Biol*. 16: 177 [10.1186/s13059-015-0734-x]
962 64. Sakamoto K, Vucenik I, and Shamsuddin AM (1993) [^{3}H]phytic acid (inositol
963 hexaphosphate) is absorbed and distributed to various tissues in rats. *J. Nutr*. 123:
964 713-720 [10.1093/jn/123.4.713].
965 65. Sahu S, Wang Z, Jiao X, Gu C, Jork N, Wittwer C, Li X, Hostachy S, Fiedler D,
966 Wang H, et al. (2020) $InsP_7$ is a small-molecule regulator of NUDT3-mediated
967 mRNA decapping and processing-body dynamics. *Proc. Natl. Acad. Sci. U. S. A.*
968 117: 19245-19253 [10.1073/pnas.1922284117].
969 66. Saiardi A (2012) How inositol pyrophosphates control cellular phosphate
970 homeostasis? *Adv. Biol. Regul*. 52: 351-359 [10.1016/j.jbior.2012.03.002].
971 67. Saiardi A, Erdjument-Bromage H, Snowman AM, Tempst P, and Snyder SH
972 (1999) Synthesis of diphosphoinositol pentakisphosphate by a newly identified
973 family of higher inositol polyphosphate kinases. *Curr. Biol*. 9: 1323-1326
974 [10.1016/s0960-9822(00)80055-x].

975 68. Saiardi A, Nagata E, Luo HR, Snowman AM, and Snyder SH (2001) Identification
976 and characterization of a novel inositol hexakisphosphate kinase. *J. Biol. Chem.*
977 276: 39179-39185 [10.1074/jbc.M106842200]
978 69. Sarmah B, and Wente SR (2010) Inositol hexakisphosphate kinase-2 acts as an
979 effector of the vertebrate Hedgehog pathway. *Proc. Natl. Acad. Sci. U. S. A.* 107:
980 19921-19926 [10.1073/pnas.1007256107].
981 70. Schell MJ, Letcher AJ, Brearley CA, Biber J, Murer H, and Irvine RF (1999) PiUS
982 (Pi uptake stimulator) is an inositol hexakisphosphate kinase. *FEBS Lett*. 461:
983 169-172 [10.1016/s0014-5793(99)01462-3].
984 71. Schneider S (2015) Inositol transport proteins. *FEBS Lett*. 589: 1049-1058
985 [10.1016/j.febslet.2015.03.012].
986 72. Shah A, Ganguli S, Sen J, and Bhandari R (2017) Inositol Pyrophosphates:
987 Energetic, Omnipresent and Versatile Signalling Molecules. *J. Indian Inst. Sci*. 97:
988 23-40 [10.1007/s41745-016-0011-3].
989 73. Shears SB (2015) Inositol pyrophosphates: why so many phosphates? *Adv. Biol.*
990 *Regul*. 57: 203-216 [10.1016/j.jbior.2014.09.015].
991 74. Shears SB (2016) Towards pharmacological intervention in inositol pyrophosphate
992 signalling. *Biochem. Soc. Trans*. 44: 191-196 [10.1042/BST20150184].
993 75. Simões-Costa MS, McKeown SJ, Tan-Cabugao J, Sauka-Spengler T, and Bronner
994 ME (2012) Dynamic and differential regulation of stem cell factor FoxD3 in the
995 neural crest is encrypted in the genome. *PLoS Genet.* 8: e1003142
996 [10.1371/journal.pgen.1003142]
997 76. Smith TH, Ngwainmbi J, Grider JR, Dewey WL, and Akbarali HI (2013) An
998 in-vitro preparation of isolated enteric neurons and glia from the myenteric plexus

of the adult mouse. *J. Vis. Exp*. 78: 50688 [10.3791/50688].

77. Subramanian A, Tamayo P, Mootha VK, Mukherjee S, Ebert BL, Gillette MA, Paulovich A, Pomeroy SL, Golub TR, Lander ES, et al. (2005) Gene set enrichment analysis: A knowledge-based approach for interpreting genome-wide expression profiles. *Proc. Natl. Acad. Sci. U. S. A.* 102: 15545-15550 [10.1073/pnas.0506580102]

78. Sun J, Nishiyama T, Shimizu K, and Kadota K (2013) TCC: an R package for comparing tag count data with robust normalization strategies. *BMC Bioinformatics* 14: 219 [10.1186/1471-2105-14-219]

79. Vera Alvarez R, Pongor LS, Mariño-Ramírez L, and Landsman D (2019) TPMCalculator: one-step software to quantify mRNA abundance of genomic features. Bioinformatics 35: 1960-1962 [10.1093/bioinformatics/bty896]

80. Vitelli F, Morishima M, Taddei I, Lindsay EA, and Baldini A (2002) Tbx1 mutation causes multiple cardiovascular defects and disrupts neural crest and cranial nerve migratory pathways. *Hum. Mol. Genet.* 11: 915-922 [10.1093/hmg/11.8.915]

81. Wilson MS, Bulley SJ, Pisani F, Irvine RF, and Saiardi A (2015) A novel method for the purification of inositol phosphates from biological samples reveals that no phytate is present in human plasma or urine. *Open Biol*. 5: 150014 [10.1098/rsob.150014].

82. Wilson MS, Jessen HJ, and Saiardi A (2019) The inositol hexakisphosphate kinases IP6K1 and -2 regulate human cellular phosphate homeostasis, including XPR1-mediated phosphate export. *J. Biol. Chem*. 294: 11597-11608 [10.1074/jbc.RA119.007848].

1023 83. Wilson MS, Livermore TM, and Saiardi A (2013) Inositol pyrophosphates:
1024 between signalling and metabolism. *Biochem. J.* 452: 369-379
1025 [10.1042/BJ20130118].
1026 84. World Medical Association (2013) World Medical Association Declaration of
1027 Helsinki: ethical principles for medical research involving human subjects. *JAMA*
1028 310: 2191-2194 [10.1001/jama.2013.281053].
1029 85. Wright CM, Garifallou JP, Schneider S, Mentch H, Kothakapa DR, Maguire BA,
1030 and Heuckeroth RO (2021) Dlx1/2 mice have abnormal enteric nervous system
1031 function. *JCI insight* 5: e131494. [10.1172/jci.insight.131494]
1032 86. Zhong S, Zhang S, Fan X, Wu Q, Yan L, Dong J, Zhang H, Li L, Sun L, Pan N, et
1033 al. (2018) A single-cell RNA-seq survey of the developmental landscape of the
1034 human prefrontal cortex. *Nature* 555: 524-528 [10.1038/nature25980]
1035
1036

Figure titles and legends

Figure 1. Refined HILIC-MS/MS analysis for IP_6 and PP-IPs

A. Effect of InfinityLab deactivator additive as a mobile phase modifier on SRM chromatograms of IP_6 and IP_7 before and after biological sample injection. 100 pmol of each synthetic analyte were injected.

B. Effect of InfinityLab deactivator additive as a mobile phase modifier on the detection of low amounts of synthetic PP-IP. 10 and 20 pmol of IP_7 standard were injected.

C. Chemical structure of IP_7 and IP_8.

D. Product ion spectrum of IP_8 (singly deprotonated precursor, left panel; doubly deprotonated precursor, right panel). Characteristic fragment ions generated by loss of water (H_2O, 18 Da) and phosphoric acid (H_3PO_4, 80 Da) are also shown.

E. Gel electrophoretic results (left panel) and SRM chromatograms (right panel) of synthetic IP_6, IP_7, and IP_8 standard. The PolyP ladder was used as an electrophoresis standard. 500 pmol of each standard were injected for LC-MS.

F. Representative SRM chromatograms of IP_6, IP_7, and IP_8 in untreated (left panel) and NaF-treated (right panel) HCT116 cell samples. The three best transitions per molecule are shown for the peak identification of each compound. Arrows indicate the SRM peak of corresponding analytes.

Figure 2. The mammalian gastrointestinal tract (GIT) contains high levels of PP-IPs

A-C. The concentrations of IP_6 **(A)** and IP_7 **(B)** and IP_7/IP_6 ratios **(C)** in the 15 organs of standard diet-fed C57BL/6J mice. The values shown are expressed as pmol per mg of organ weight (n = 4).

D. Representative SRM chromatograms of IP_7 and IP_8 in stomach and small intestine samples of standard diet-fed C57BL/6J mice. The three best transitions per molecule are shown for the peak identification of each compound. The arrows indicate the SRM peaks of the corresponding analytes.

E. Representative SRM chromatograms of IP_7 in CNS samples of standard diet-fed C57BL/6J mice.

F. Photographs (left) and SRM chromatograms of IP_6, IP_7, and IP_8 (right) of standard diet (CE-2) and the two different purified diets (iVid-neo and 70% casein).

G. Relative concentrations of IP_6 and PP-IPs in the standard and purified diets. The values shown represent the mean ± standard deviation (SD) of three independent experiments and are expressed relative to those of the standard diet. Asterisks indicate statistical significance ($P < 0.05$, Student's t-test) compared with the standard diet.

H. Representative SRM chromatograms of IP_6 and IP_7 in the feces of standard diet-fed C57BL/6J mice.

I. Relative concentrations of IP_6 and IP_7 in the feces of standard diet-fed C57BL/6J mice. The values shown are expressed relative to those of the standard diet (n = 3). Asterisks indicate statistical significance ($P < 0.05$, Student's t-test) compared with the standard diet.

J. IP_7/IP_6 ratio in standard diet and feces of standard diet-fed C57BL/6J mice (n = 3). n.s., not significant (Student's *t*-test).

Figure 3. Enhanced IP_7 metabolism is retained in the proximal GIT of rodents under conditions of depleted dietary IP_6 and PP-IP supply

A. Schematic illustration of the experimental workflow. C57BL/6J mice were fed a

standard diet (n = 3) or purified diet (iVid-neo) for 2 months (n = 4) or fasted for 48 h (n = 4).

B, C. The concentrations of IP_6 **(B)** and IP_7 **(C)** in the CNS, testes, and GIT of C57BL/6J mice under the three different conditions. The values shown are expressed as pmol per mg of organ weight.

D. Representative SRM chromatograms of IP_7 in the GIT of C57BL/6J mice fed with purified diet (left panel) or under fasting conditions (right panel). Arrows indicate the SRM peak of IP_7.

E. IP_7/IP_6 ratios in the CNS, testes, and GIT of C57BL/6J mice under the three different conditions. Asterisk indicates statistical significance ($P < 0.05$, one-way ANOVA, Bonferroni-type post-hoc test) compared with the standard diet-fed mice.

F. Graphical scheme of the experiment. Sprague–Dawley rats were fed a standard (n = 3) or purified diet (70% casein) for 1 month (n = 3).

G-I. Concentrations of IP_6 **(G)**, IP_7 **(H)** and IP_7/IP_6 ratios **(I)** in the CNS, testes, and GIT of the rats under the two different conditions. The values shown are expressed as pmol per mg of organ weight.

Figure 4. Enteric neurons highly express IP6K2 in the mammalian GIT

A. Expression analysis of IP6K1-3 in intestinal cell subsets using publicly available scRNA-seq datasets. Relative expression (log scale) of IP6K1-3 among human embryonic enteric cells (left) and their neural cell subsets (right), obtained by analysis of human embryonic intestinal cells scRNA-seq datasets are shown (Fawkner-Corbett et al, 2021). The size and color of the dots represent the percentage of cells which express IP6K1-3 mRNA and their average abundances within a cluster, respectively.

B. UMAP-based unsupervised clustering of recently reported mouse embryonic (E18.5) ENS data (Morarach et al, 2021) (upper panel). Assignment of cell identities was based on the expression of signature genes as described in the literature: *Sox10* (Progenitor), *Ascl1* (Neuroblast), *Elavl4* (Neuron), *Plp1* (Enteric glia) and *Dhh* (SCP). Relative expression (log scale) of IP6K1-3 among the ENS clusters (lower panel) are shown. ENS, enteric nervous system; SCP, Schwann cell precursor; E, embryonic day; UMAP, uniform manifold approximation and projection.

C. Immunohistochemical analysis of IP6K2 expression in the duodenal muscularis externa of C57BL/6J mice. Three different areas of confocal microscopy images are shown. The neuronal marker HuC/D was also detected to identify enteric neurons in the myenteric plexuses. Open arrowheads indicate double-positive cells. DIC images were overlaid onto the respective merged fluorescent images to identify cell contours. DIC, differential interference contrast. Scale bar = 10 μm.

Figure 5. *IP6K2*$^{-/-}$ mice show significant impairment of IP$_7$ metabolism in the proximal GIT

A. Schematic depiction of the *IP6K2* genomic locus in *IP6K2*$^{-/-}$ and WT mice (upper panel) and the experimental workflow (lower panel). IP6K2 exons and introns are represented as boxes and lines, respectively.

B. IP6K2 mRNA levels in the CNS and GIT of *IP6K2*$^{-/-}$ and WT mice (upper left panel). The values shown are normalized with 18S rRNA level and expressed as copies per μg RNA (n = 3). Electrophoretic gel images of qPCR products (lower left panel) and PCR primer location in the *IP6K2* genomic locus (right panel) was also depicted. W, WT; K, *IP6K2*$^{-/-}$; n.d., not detected; *, non-specific band.

C. Representative Western blot image of IP6K1 and IP6K2 expression in the cerebrum of *IP6K2*$^{-/-}$ and WT mice. β-actin was used as the internal control.

D-F. The concentrations of IP_6 **(D)** and IP_7 **(E)**, and IP_7/IP_6 ratios **(F)** in the CNS, GIT, and other organs of *IP6K2*$^{-/-}$ and WT mice. The values shown represent the mean ± SD of five independent experiments and are expressed as pmol per mg of organ weight. Asterisks indicate statistical significance ($P < 0.05$, Student's *t*-test) compared with WT mice.

G, H. Representative SRM chromatograms of IP_6 (upper panel) and IP_7 (lower panel) in the stomach **(G)** and duodenum **(H)** of *IP6K2*$^{-/-}$ and WT mice. The three best transitions per molecule are shown for peak identification of each compound. Arrows indicate the SRM peak of each analyte.

Figure 6. IP6K2-dependent enhanced IP_7 metabolism exists in the gut and duodenal muscularis externa where the myenteric plexus is located

A. Schematic illustration of the experimental workflow. C57BL/6J mice were fed a standard diet, or fasted for 48 h. These mice were sacrificed to collect four stomach and 3 consecutive 5-cm segments of the proximal GIT (duodenum, jejunum, ileum). The muscularis externa containing myenteric plexus as well as total tissues in the proximal GITs were subjected to HILIC-MS/MS analysis.

B-D. The concentrations of IP_6 **(B)**, IP_7 **(C)**, and IP_7/IP_6 ratios **(D)** in the muscularis externa and total tissue of four proximal GIT segments of C57BL/6J mice under the two different conditions. The values shown represent the mean ± SD of four independent experiments and are expressed as pmol per mg of organ weight.

E. Whole mount immunostaining of WT and *IP6K2*$^{-/-}$ duodenal muscularis externa

using anti-neuronal markers antibodies. Two different areas of confocal microscopic images of each neuron marker are shown. The neuronal markers HuC/D and βIII-tubulin were detected to identify enteric neuronal somas and enteric nerve fibers in the myenteric plexuses, respectively. Scale bar = 50 μm.

F. The concentration of enteric neurons in WT and *IP6K2*$^{-/-}$ duodenal muscularis externa. The values shown represent the mean ± SD of three independent experiments and are expressed relative to those of WT mice. n.s., not significant (Student's *t*-test).

G. Schematic illustration of the experimental workflow. *IP6K2*$^{-/-}$ and WT mice fasted for 48 h were sacrificed to collect four proximal GIT segments (stomach, duodenum, jejunum, ileum), which were then subjected to isolate muscularis externa.

H-J. The abundances of IP_6 **(H)** and IP_7 **(I)**, and IP_7/IP_6 ratios **(J)** in the muscularis externa of the four GIT segments of *IP6K2*$^{-/-}$ and WT mice. The values shown represent the mean ± SD of four independent experiments and are expressed relative to those for WT mice. Asterisks indicate statistical significance ($P < 0.05$, Student's *t*-test) compared with WT mice.

Figure 7. IP6K2-IP_7 axis is crucial for certain neurotranscriptome profile associating with ENS development and functioning

A. Transcript levels of two different neuronal genes (*Ddr5* and *Cckbr*) in the CNS and GIT of *IP6K2*$^{-/-}$ and WT mice. Data were normalized to 18S rRNA level. The values shown represent the mean ± SD of three (CNS of *IP6K2*$^{-/-}$, and CNS and GIT of WT mice) and five (GIT of *IP6K2*$^{-/-}$ mice) independent experiments and are expressed relative to those of WT mice. Asterisks indicate statistical significance ($P < 0.05$, Student's *t*-test) compared with WT mice.

B. Schematic illustration of the experimental workflow. *IP6K2*$^{-/-}$ and WT mice were sacrificed to collect the duodenal muscularis externa. High-quality total RNAs isolated from these tissues (each n =3) were subjected to whole transcriptome analysis by high-throughput RNA sequencing.

C. Gene Set Enrichment Analysis (GSEA) of the enriched gene signature in *IP6K2*$^{-/-}$ duodenal muscularis externa. Cell type signature gene sets (C8 in The Molecular Signatures Database ver7.5.1; http://www.gsea-msigdb.org/gsea/msigdb/index.jsp) were used for this analysis. Horizontal dashed line indicates nominal P-value 0.05, and vertical lines indicate normalized enriched score (NES)□± 1.2 cutoff. Gene sets assigned to neural progenitor cells and oligodendrocyte progenitor cells (source data is derived from Zhong et al, 2018), neural stem cells and glial cells (Fan et al, 2018), and mature neurons (inhibitory neurons, Cao et al, 2020; GABAergic and dopaminergic neurons, La Manno et al, 2016) with nominal $P < 0.05$ and $NES > 1.2$ or < -1.2 are labeled in colored dots.

D. Representative GSEA plots of the gene sets enriched among up-regulated (inhibitory neurons, GABAergic neurons, dopaminergic neurons) or down-regulated (neural progenitor cells, neural stem cells, glial cells) genes by genetic ablation of *IP6K2* in the duodenal muscularis externa.

E. Normalized expression levels (transcripts per million, TPM) from RNA-seq data for 7 neuronal genes prominently and significantly ($P < 0.05$, Student's *t*-test) accumulated or depleted in *IP6K2*$^{-/-}$ duodenal muscularis externa compared with WT counterparts (n = 3).

F. Validation of RNA-seq results by qPCR. Data were normalized to β-actin level. The values shown represent the mean□±□SD of six independent experiments and are

expressed relative to those for WT mice. Asterisks indicate statistical significance ($P < 0.05$, Student's *t*-test) compared with WT mice.

G. Transcript levels of three different neuronal genes (*Ddr5*, *Cckbr* and *Npy4r*) in the duodenal muscularis externa of *IP6K2*$^{-/-}$ and WT mice. Data were normalized to β-actin level. The values shown represent the mean ± SD of six independent experiments and are expressed relative to those for WT mice. Asterisks indicate statistical significance ($P < 0.05$, Student's *t*-test) compared with WT mice.

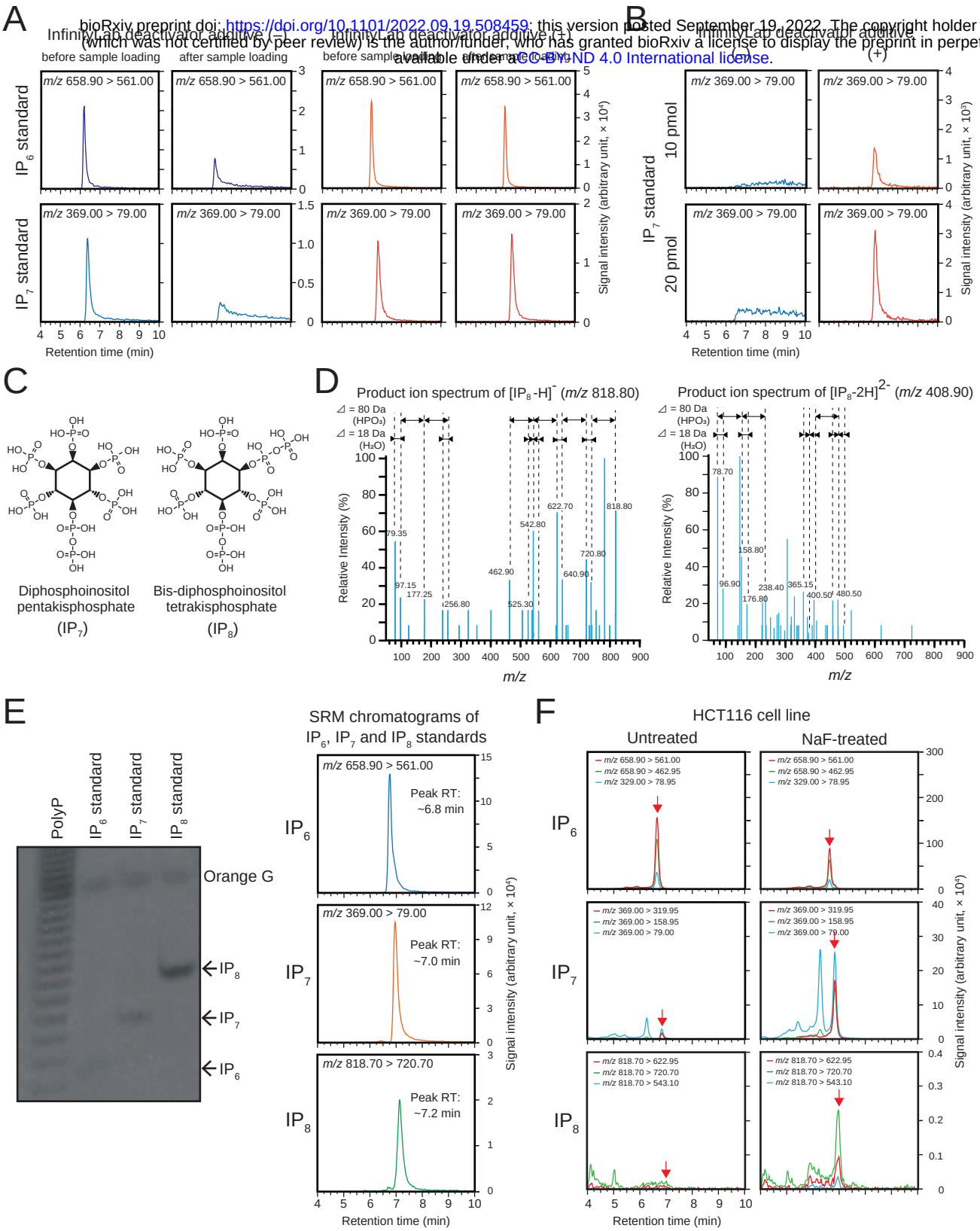

Fig 1. Ito et al.

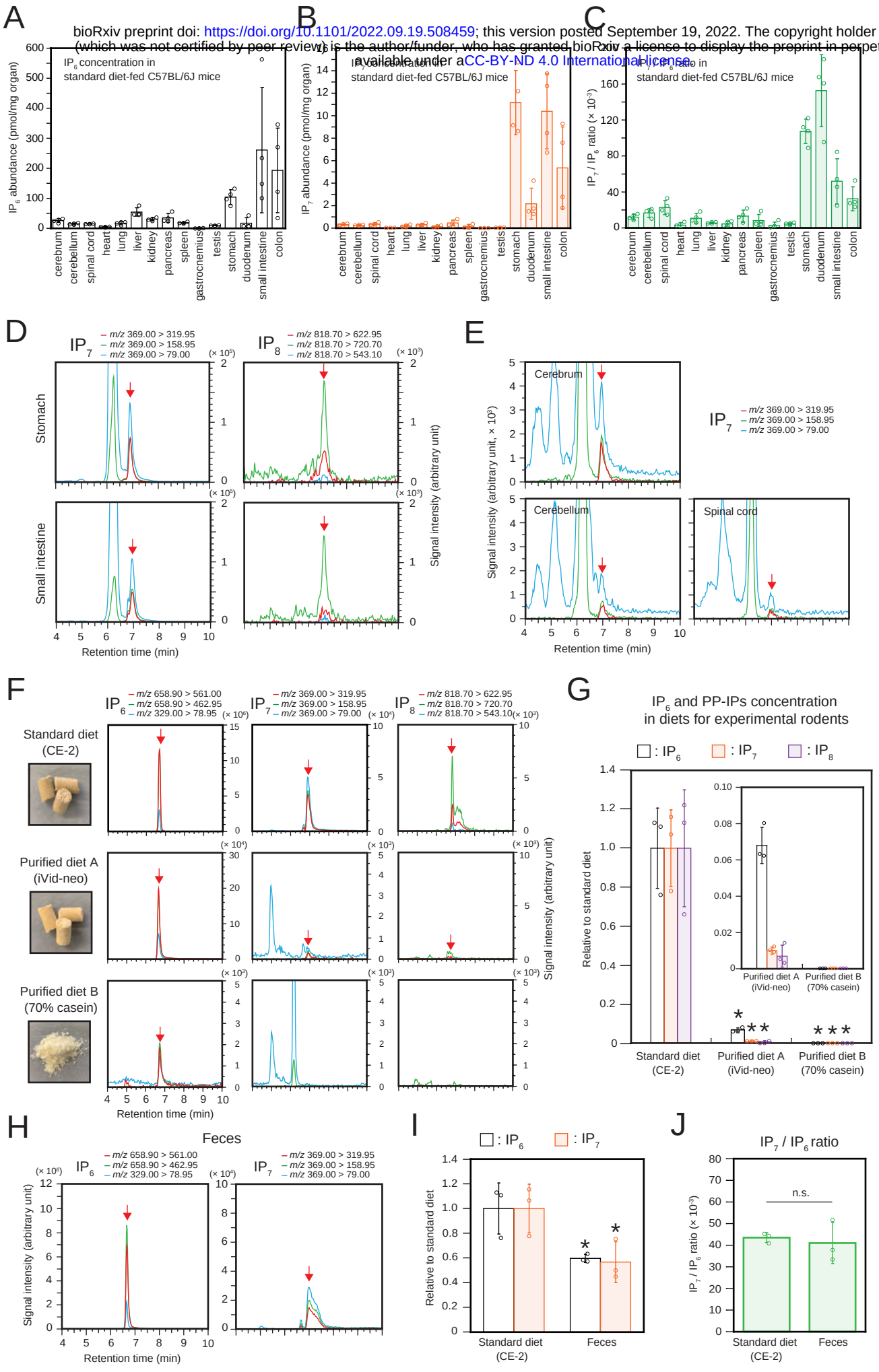

Fig 2. Ito et al.

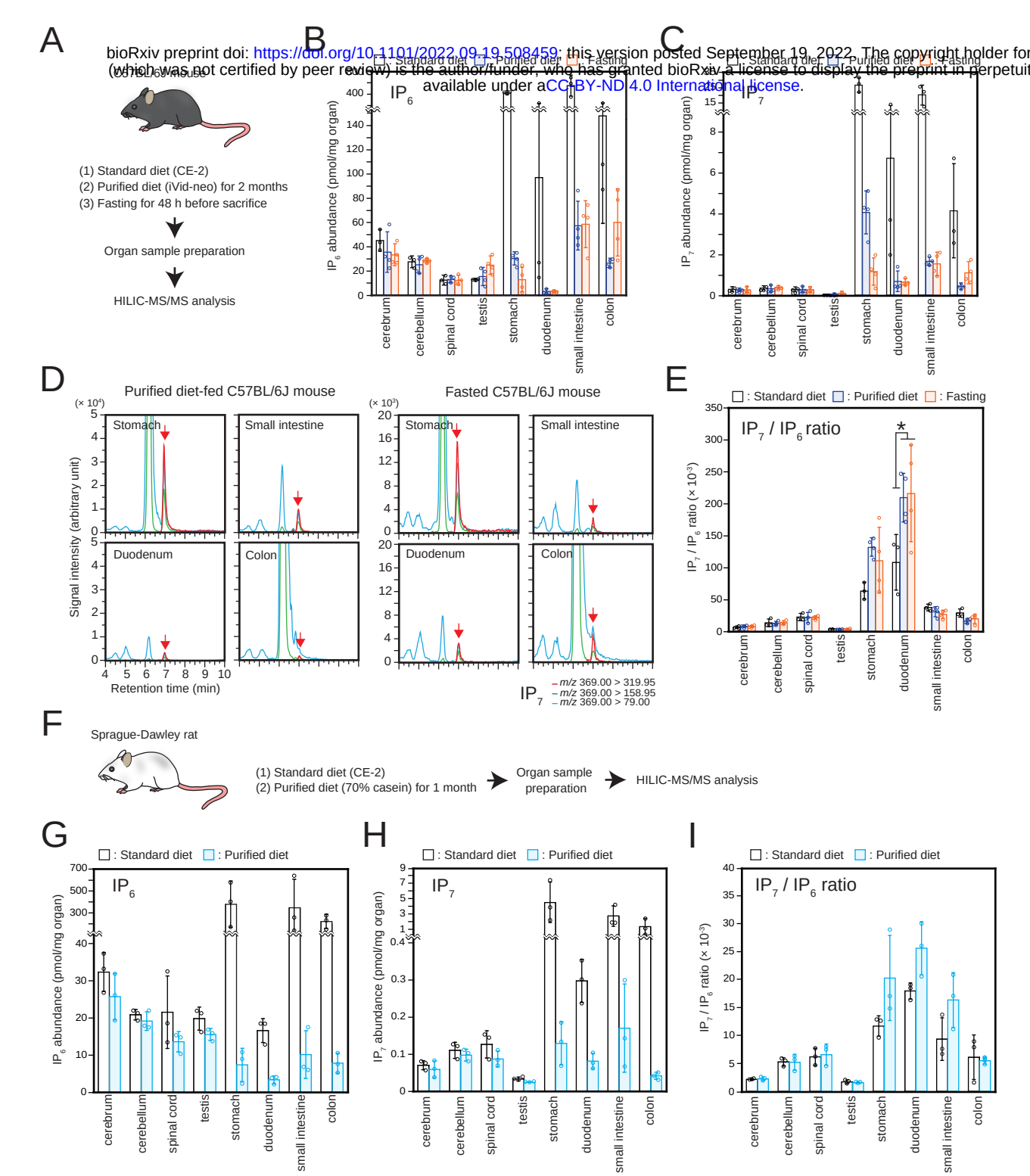

Fig 3. Ito et al.

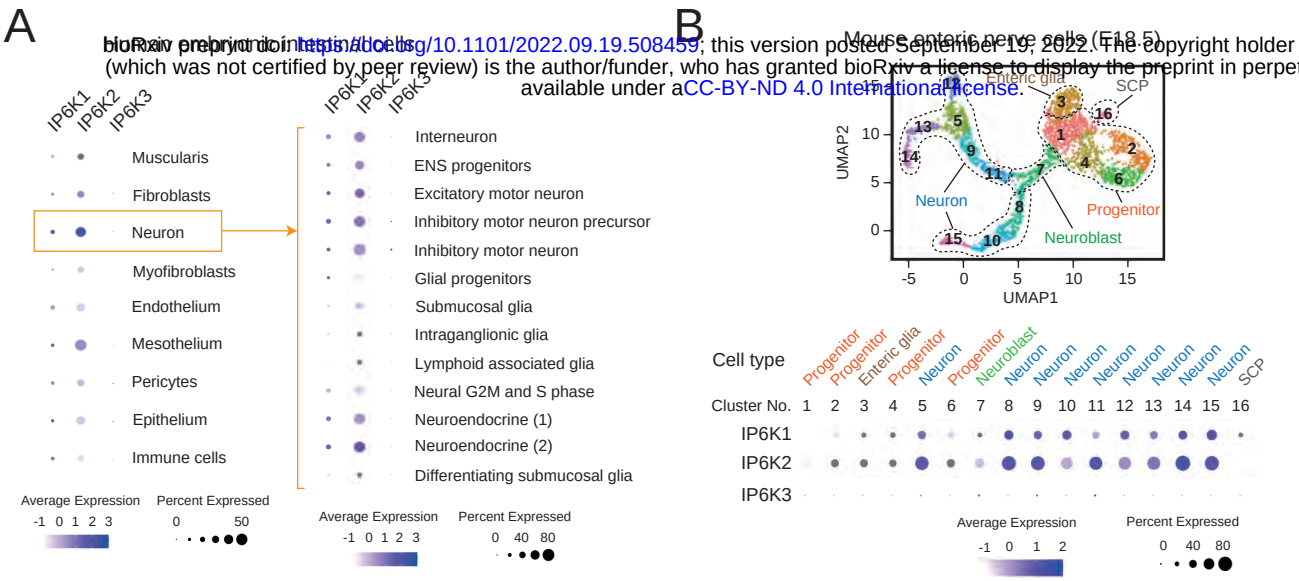

Fig 4. Ito et al.

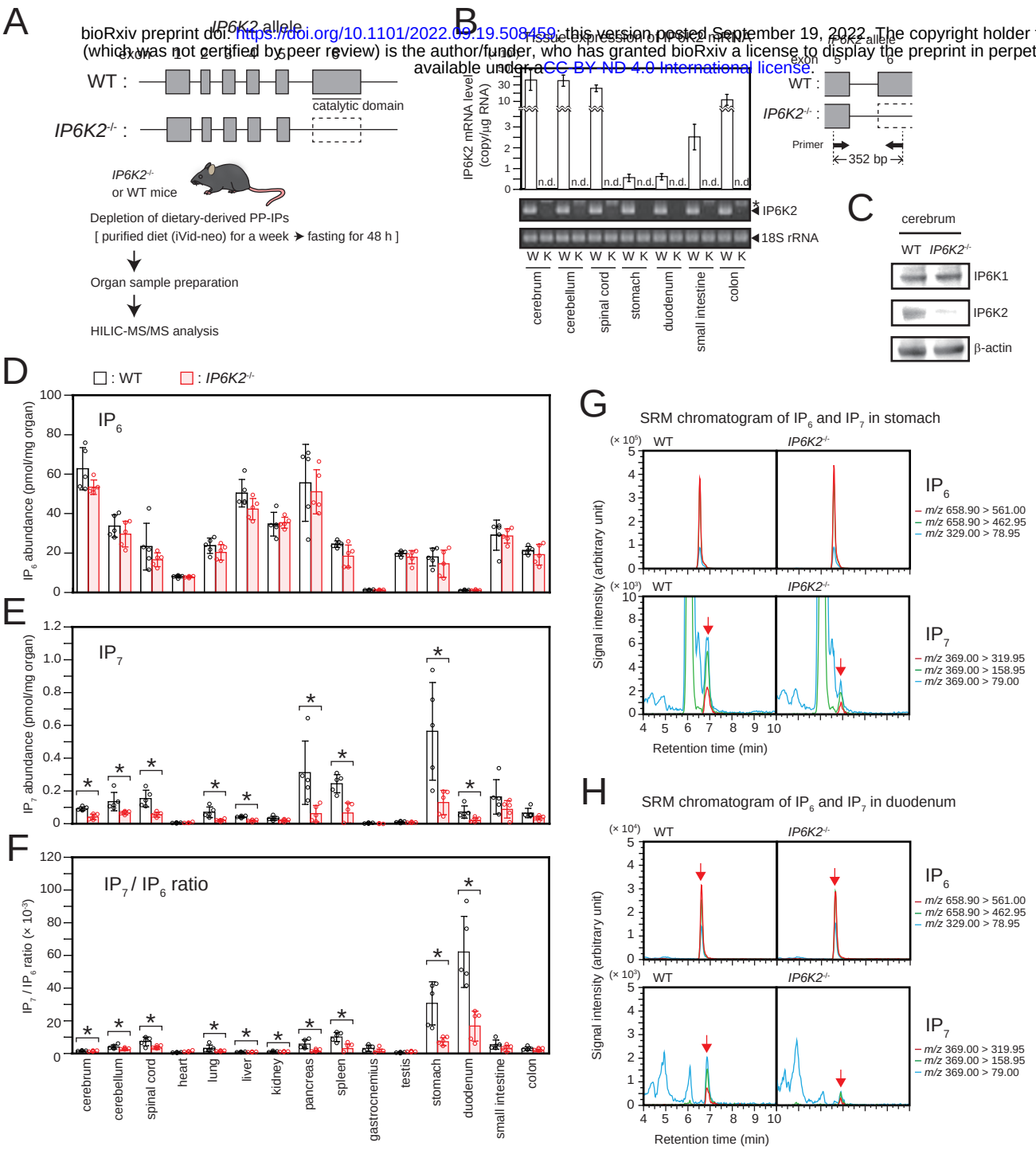

Fig 5. Ito et al.

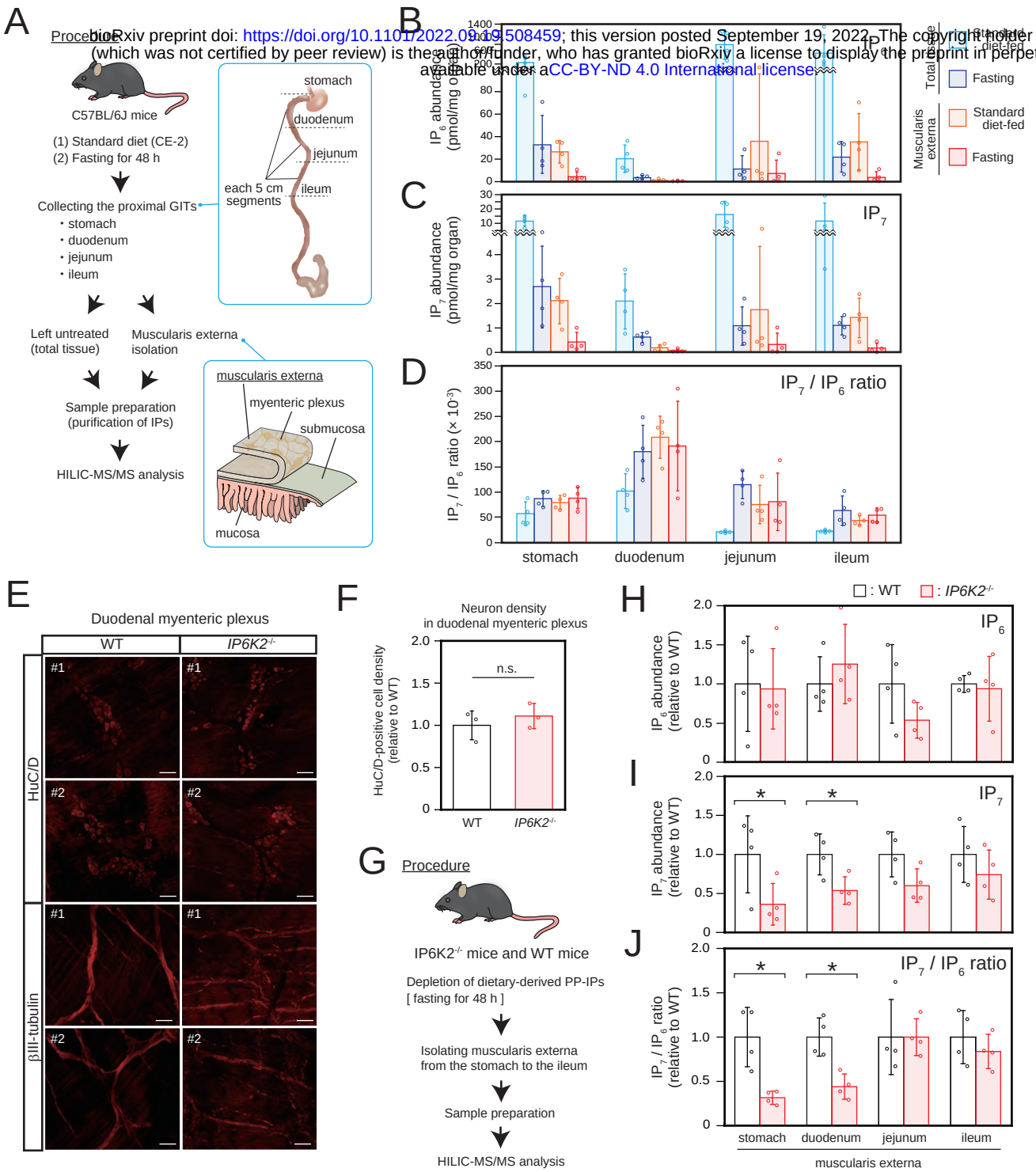

Fig 6. Ito et al.

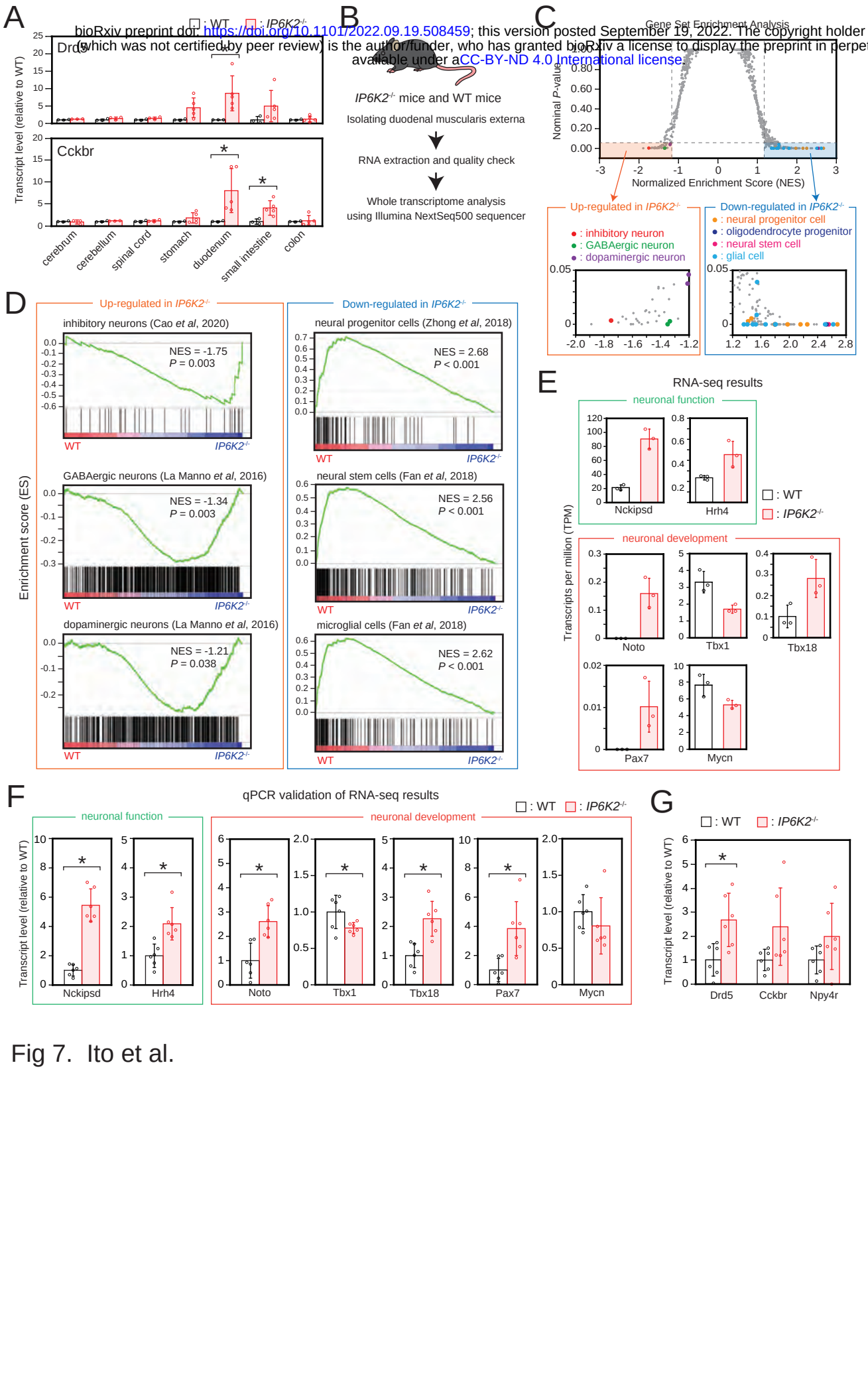

Fig 7. Ito et al.